Developing metabolomics for a systems biology approach to understand Parkinson's disease

Willacey, C.C.W.

Chapter 5

Mechanistic model-driven exometabolomic characterisation of human dopaminergic neuronal metabolism

German Preciat[*], Jennifer Modamio[*], Cornelius C.W. Willacey[*], Agnieszka Wegrzyn, Edinson L. Moreno, Fatima L. Monteiro, Diana El Assal, Miguel A.P. Oliveira, Can Gulersonmez, Laurent Heirendt, Zhi Zhang, Ben Cousins, Hulda S. Haraldsdóttir, Susanne Zach, Siham Hachi, Amy Harms, Santosh Vempala, Bastian Hengerer, Jens C. Schwamborn, Enrico Glaab, Ines Thiele, Thomas Hankemeier[†] and Ronan M.T. Fleming[†]

In preparation

[#†] Authors equally contributed to the manuscript

Abstract

Patient-derived cellular models are a powerful approach to study human disease, especially neurodegenerative diseases, such as Parkinson's disease, where affected primary neurons, e.g., substantia nigra dopaminergic neurons, are almost inaccessible. Induced pluripotent stem cell-derived models of midbrain-specific dopaminergic neurons are increasingly used to investigate Parkinson's disease. Starting with the comprehensive generic reconstruction of human metabolism, Recon3D, we generated the first constraint-based, genome-scale, *in silico* model of human dopaminergic neuronal metabolism (iNESC2DN). Transcriptomic data, obtained by RNA sequencing, and quantitative exometabolomic data, obtained by targeted mass spectrometry-based metabolomics were generated for *in vitro* neuroepithelial stem cell-derived cultures and supplemented by extensive manual curation of the literature on dopaminergic neurons. The predictions of the iNESC2DN model are consistent with neurobiochemical prior information and in concordance with measured fluxes of uptake and secretion of many extracellular metabolites by dopaminergic neurons *in vitro*. We leverage it to rank order the most important metabolite concentrations to quantify to maximally reduce the uncertainty associated with current predictions of normal dopaminergic neuronal metabolism *in vitro*, as well as optimally design experiments to measure metabolic perturbations associated with Parkinson's Disease. Finally, the iNESC2DN model provides a foundation for future targeted metabolomic and tracer-based metabolomic analyses of dopaminergic neurons. This illustrates the synergy between constraint-based computational modelling of metabolism and biology-driven quantitative bioanalytical chemistry.

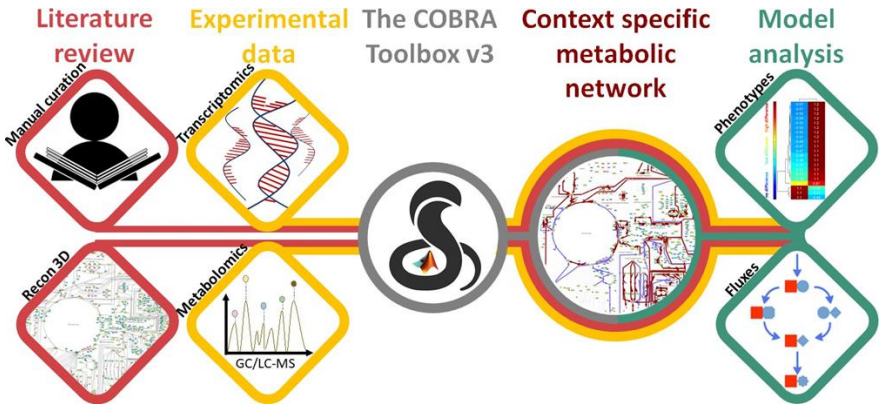
Literature review
Experimental data
The COBRA Toolbox v3
Context specific metabolic network
Model analysis
Manual curation
Transcriptomics
Recon 3D
Metabolomics
GC/LC-MS
Phenotypes
Fluxes

Background

Patient specific induced pluripotent stem cells (iPSCs)-derived, neuroepithelial stem cells (NESC)[39, 46, 6, 17], differentiated into neurons[33], offer an accessible approach to study neurodegenerative disorders *in vitro*. These neurons exhibit certain features, such as extensive arborisation and spontaneous electrophysiological activity[19], that mimic nigrostriatal dopaminergic neurons, the cell type most vulnerable to degeneration in Parkinson's Disease (PD) [25]. It has been hypothesised that this selective vulnerability is due to an imbalance between the high energy demand of, for example, maintaining tonic electrophysiological activity, and low energy supply as a result of, for example, mitochondrial dysfunction[29,7]. Therefore, characterisation of the normal metabolic status of a dopaminergic neuron is of major interest but has not yet been reported.

COnstraint-Based Reconstruction and Analysis (COBRA)[28] provides a mathematical and mechanistic computational modelling framework for experimental design, integrative analysis of prior biochemical knowledge with experimental data as well as the generation of novel hypotheses. In particular, quantitative bioanalytical chemistry[27, 35, 32] has been effectively combined with constraint-based modelling of metabolism[3] to enable context-specific biochemical interpretation of metabolomic data, e.g., to discover differences in glycolytic versus oxidative metabolism in different lymphoblastic leukaemia cell lines[4], and to characterise metabolic changes influencing pluripotency and cell fate in stem cells[9].

In this study, Recon3D[8], the most comprehensive generic human metabolic reconstruction to date, was rendered context-specific by a combination of manual curation and omics data integration, to generate a constraint-based model of metabolism in human neuroepithelial stem cell-derived dopaminergic neurons, denoted iNESC2DN. Manual literature curation and transcriptomic data were used to establish the activity, or inactivity, of a core set of metabolic genes and reactions. In parallel, liquid chromatography-mass spectrometry (LC-MS) and gas chromatography-mass spectrometry (GC-MS) were used to quantify biogenic amines and organic acids in fresh and spent culture media from NESC-derived dopaminergic neurons in macroscopic cell culture. Different subsets of the obtained exometabolomic data, were used to refine the iNESC2DN model and test its predictions. The predicted metabolite uptake and secretion fluxes of the iNESC2DN

model were broadly consistent with bioanalytical quantification of metabolite consumption and secretion fluxes. A novel approach was developed to predict the most informative extracellular metabolites to target for future bioanalytical quantification as well as predict the effect of condition-specific metabolic perturbations as a mean to design future targeted metabolomic and tracer-based metabolomic experiments. Taken together, the iNESC2DN model provides a foundation for a systems approach to investigate metabolic dysfunction in patient-derived cellular models of PD, and the approach taken can serve as a template for the study of other neurodegenerative diseases.

Materials and methods

The following summary is complemented by essential methodological details as Supporting Information.

***In vitro* experiments.** The iPSC derived NESC were differentiated towards midbrain-specific dopaminergic neurons using an established protocol[33]. Calcium imaging and automated image analysis using an established pipeline[19] was used to assess electrophysiological activity at day 23 of differentiation (Figure S4). Additionally, at day 23 of differentiation, transcriptomic and exometabolomic data were generated from separate *in vitro* cultures using the same differentiation protocol[33] (Figure S4). Transcriptomic data was obtained by RNA-sequencing. Targeted exometabolomic data was generated from fresh and spent culture media, for 74 biogenic amines and amino acids, using an established LC-MS method[24], and for 24 organic acids by adapting an established GC-MS platform[1] (supplementary information section S1).

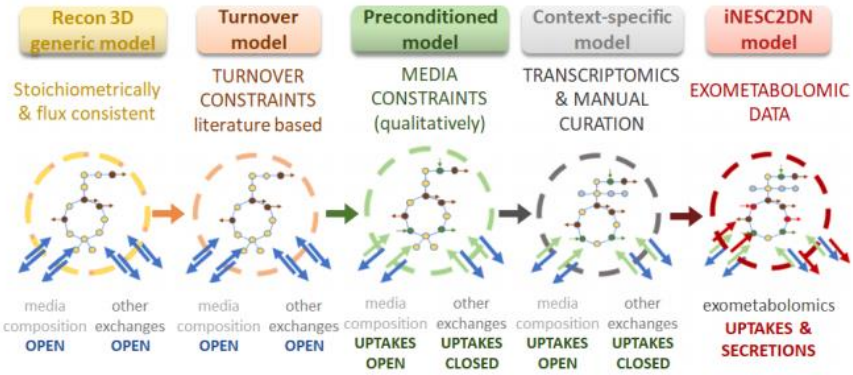

Figure 5.1: ***Overview of the model generation pipeline.*** *From the Recon3D metabolic model[8], a turnover model was generated by the integration of constraints representing the minimum cellular turnover of key metabolites. A preconditioned model was then generated by applying qualitative media constraints. Transcriptomic and manually curated data revealed the active and inactive reactions and genes in the cell culture and in dopaminergic neurons, which were integrated to generate a context-specific model using a model extraction algorithm[43]. The final iNESC2DN model, used for design of future experiments, includes all exometabolomically derived constraints on uptake and secretion reactions.*

Reconstruction. Following an established protocol[40], the generic human metabolic reconstruction, Recon2[41], was refined with additional manual curation of metabolic literature specific to dopaminergic neurons, and included in an update to the generic human metabolic reconstruction, Recon3D[8]. Further manual curation was performed to define active and inactive reactions and genes, transport reactions, degradation pathways and quantitative constraints necessary to represent the requirement for molecular turnover in a non-growing, non-dividing dopaminergic neuron. When specific information on dopaminergic neurons was not present in the literature, information from other neuronal types, cerebral tissue, or rodent data was used (supplementary information section S2).

Model generation. A stoichiometrically consistent, flux consistent, constraint-based metabolic model, specific to *in vitro* NESC-derived dopaminergic neurons, was generated using the results of manual curation combined with transcriptomic and

exometabolomic data. Active and inactive genes, obtained from manual curation, or transcriptomic data, or both, were constrained in Recon3D, with manual curation given priority if a discrepancy arose[40]. This integration was completed using the COBRA Toolbox[16], a software tool for modelling genome-scale biochemical networks and integrative analysis of omics data in a network context. In particular, FASTCORE[43], was used as the model extraction algorithm. Models were refined by comparing biochemical literature with the results of Flux Balance Analysis[26]. The workflow for model generation is illustrated in Figure 5.1 and described in more detail in supplementary information section S3 and section 4.

Model testing. Two test models were generated, termed ModelUpt and ModelSec, which included a subset of quantitative metabolomic data as constraints on uptake reaction fluxes or secretion reaction fluxes, respectively, while the excluded metabolomic data was used for comparison with model predictions. Flux Variability Analysis (FVA)[20] and uniform sampling[15], were used to test the ability of these test models to predict the fluxes of extracellular secretion or uptake reactions, or both (supplementary information section S5). Uniform sampling provides a quantitative prediction of the probability of each quantitative flux value, between the same minimum and maximum flux predicted by flux variability analysis, assuming that each feasible steady-state flux vector is equi-probable.

Experimental design. Three distinct pipelines were developed that use the iNESC2DN model for experimental design. An *uncertainty reduction* pipeline rank orders exchanged metabolites according to those whose quantitative exometabolomic measurement would maximally shrink the feasible steady-state solution space. A *phenotypic perturbation* pipeline rank orders exchange reactions according to those whose rates are predicted to be most likely to change in response to a perturbation to an internal reaction rate. Finally, *a tracer-based metabolomic* pipeline was used to identify the non-elementary conserved moieties[14] exchanged across the boundary of the iNESC2DN model that could be isotopically labelled to quantify the activity of metabolic pathways of specific importance to dopaminergic neurons (supplementary information section S6).

Results

Experimental characterisation. Differentiated neurons were identified by TUBβIII immunoreactivity and those also positive for tyrosine hydroxylase indicated the presence of neurons capable of converting tyrosine to L-DOPA, the penultimate step in dopamine synthesis (Figure 5.6a). Analysis of calcium imaging data revealed spontaneously active neurons (Figure 5.6b, c, d). In the transcriptomic data, fragments were detected from 18,530 genes, but only 12,698 of these were sufficiently abundant to be considered expressed. That is, above a threshold of one Fragment per Kilobase of exon per Million reads[34]. Of the expressed genes, 1,202 could be mapped to metabolic genes in Recon3D and were considered active, unless manual curation of the literature revealed otherwise. The selected metabolomic platforms target a total of 98 metabolites present in Recon3D. In the spent medium, only 50 metabolites were quantified above the lower limit of detection. However, the iNESC2DN model contains 49 metabolites with constraints on their corresponding exchange reaction fluxes as there was one two measured metabolite (Glutaric acid) that could not be integrated with the model as there are no stoichiometrically and flux consistent reactions that correspond to them in Recon3D (supplementary information section S7).

Dopaminergic neuronal reconstruction and model generation. Literature curation revealed evidence for the activity, or inactivity, of 252 metabolic genes (Table S-1) and 445 metabolic reactions (Table S-2) in dopaminergic neurons. Turnover constraints were added to represent the maintenance of a dopaminergic neuron (supplementary information section S4.3, Table S-2). Subsequently, differences in metabolite concentrations over time, were either converted into constraints on exchange reaction fluxes to generate a context-specific model, or kept independent from the model generation pipeline and used to test *in silico* model predictions (supplementary information section S7). Exometabolomic concentration changes for two metabolites (L-proline and serine), could not be directly integrated with the draft context-specific model as it became infeasible, therefore, as described in supplementary information section S4.6, relaxation of exometabolomic constraints on reactions corresponding to these two metabolites was required. The iNESC2DN model, i.e., the context-specific model using all exometabolomic constraints compatible with a feasible model, consists of 1,791 biochemical

reactions, between 828 unique metabolites, representing the activity of 1,853 metabolic genes from 90 biological pathways. In addition, the model contained 246 exchange reactions, 20 for uptake of metabolites from the media, 161 to secrete metabolites into spent media, 63 reversible exchange reactions (e.g., for transport of water), which were open, and 5 ionic external reactions, e.g., for sodium, calcium and potassium (Table S-3), which were closed as the model currently ignores ion transport associated with electrophysiolgical activity.

Model testing. A model generated using quantitative exometabolomic data on the uptake of metabolites (ModelUpt) could reasonably well quantitatively predict the flux of most secretion reactions, determined from exometabolomic data on metabolite secretion. Likewise, a model constrained with exometabolomic data on secretion reactions (ModelSec) could reasonably well predict the flux of most uptake reactions, determined from exometabolomic data. In both cases, the peak of the sample distribution for each exchange reaction, obtained from uniform sampling, was substantially better at quantitatively predicting the independent exometabolomic data, when compared with the ranges of exchange fluxes determined by flux variability analysis. Figure 5.2 illustrates representative comparisons for either uptakes or secretions, while Figures S12 and S13 illustrate comparisons for all reactions. In Figure 5.2, the measured secretion reaction fluxes were within the range predicted by flux variability analysis of ModelUpt for 26 metabolites, as in (a) and (b), and outside the range for 3 metabolites, as in (c). The measured uptake reaction fluxes were within the range predicted by flux variability analysis of ModelSec for 14 metabolites, as in (d) and (e), and outside the range for 5 metabolites, as in (f).

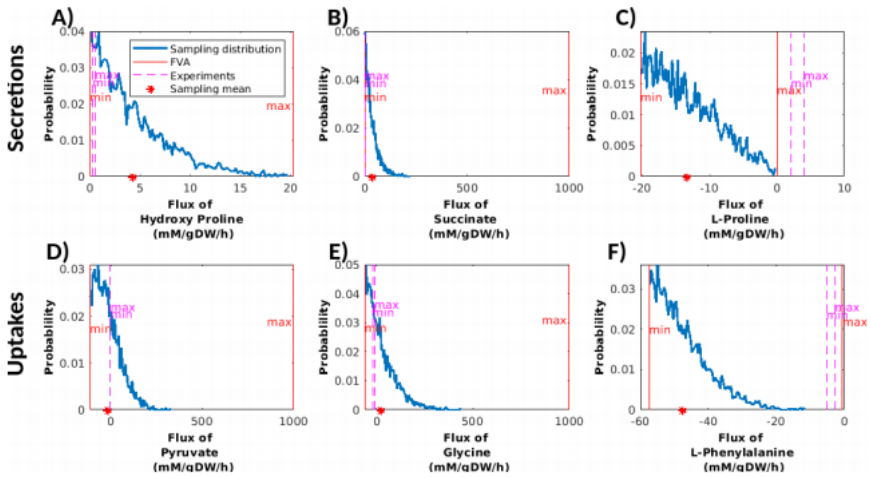

Figure 5.2: ***Comparison of predicted and measured metabolite exchange reaction rates.*** *An uptake constrained model (ModelUpt) was tested for its ability to predict measured rates of 30 secreted metabolites, with three representatives illustrated in (a-c). A secretion constrained model (ModelSec) to test its ability to predict measured rates of 19 metabolites taken up from the fresh medium, with three representatives illustrated in (d-f). A measured range for each exchange reaction rate (pink) was obtained from quantitative exometabolomic measurements and includes one standard deviation of measurement uncertainty. Predicted probability of exchange reaction flux obtained by uniform sampling (dark blue). Predicted exchange reaction flux, derived from the mean of the sampling distribution (red star). Predicted maximum and minimum fluxes obtained by flux variability analysis (FVA).*

5

Model characterisation. The iNESC2DN model has the potential to secrete 161 metabolites (Table S-2), including hydrophilic metabolites such as sugars, amino acids, carboxylic acids, keto acids, and nucleobases/nucleosides/nucleotides, while the lipophilic metabolites include free fatty acids, oxylipins, sterol lipids, sphingolipids, prenol lipids and fat soluble vitamins. The properties of these metabolites are an analytical chemistry consideration when selecting or developing targeted platforms for future exometabolomic experiments (Table S-3). Out of 161 metabolites predicted to be secreted, 17 were expected based on their assignment as active reactions during manual curation (Table S-2). A minimal set of reactions required to satisfy the constraints on the iNESC2DN model, e.g., turnover constraints,

is predicted to consist of 363 reactions (Table S-2). These reactions are involved in major metabolic pathways and pathways specific to neurons and dopaminergic neurons (Figure S14). Of the minimal reactions, about half (151/363) were manually curated to be active in dopaminergic neurons, with 32 involved the metabolism of dopamine. Twenty minimal reactions correspond to exchange reactions including 7 metabolites that can be taken up or secreted. The other 13 minimal uptake reactions predict the set of minimal medium metabolites for an *in vitro* dopaminergic neuron. These metabolites are glucose, the major source of energy, inorganic phosphate, ammonia, reduced glutathione, hydrogen carbonate and 15 amino acids, 9 of which are essential. Two amino acids, glutamine and arginine, are predicted to be conditionally essential with respect to dopaminergic neurons, as their uptake is essential for the feasibility of the model, but they can be synthesised by other tissues in the human body.

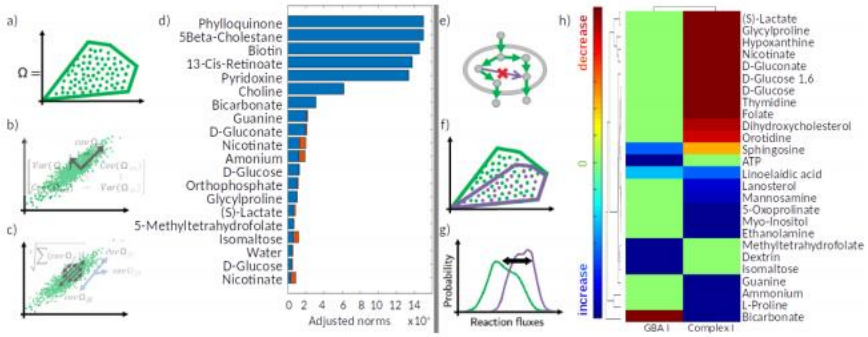

Figure 5.3: ***Experimental design.*** *Uncertainty reduction. a) The steady-state flux space,* $\Omega := \{v \in \mathbb{R}n \mid Sv = 0, l \leq v \leq u\}$*, of the iNESC2DN model was sampled. b) The covariance matrix of the sampled flux vectors* $v \in \Omega$ *was computed*. c) *The Euclidean norm for each row of the covariance matrix was calculated. d) The most informative exchange metabolites to measure were rank ordered by decreasing size of the Euclidean norm(blue), after taking into account the reduction in uncertainty (red) associated with measurement of higher ranked metabolites. The variance reduction due to cumulative measurement of higher ranked metabolite exchanges (orange) is taken into account in the ranking. Phenotypic perturbation. e) In the iNESC2DN model, certain internal reaction rates were perturbed, by changing reaction bounds, to represent, e.g., a gene deletion or a decrease in the maximum rate of a reaction. f) The steady-state flux space of the original and perturbed models are sampled. g) A two-sample Kolmogorov-Smirnov test was used to test for significant differences between the control and perturbed flux probability distributions. h) Significantly perturbed reactions were hierarchically clustered according to the magnitude of the increase (blue) or decrease (red), in the mean of the flux probability distribution for each exchanged metabolite.*

Exometabolomic experimental design. Using the uncertainty reduction pipeline, we rank ordered 20 unmeasured exchange metabolites by the degree to which their measurement would shrink the feasible set of steady-state flux vectors for the iNESC2DN model (Figure 5.3a and Table S-3). The three top informative extracellular metabolites identified were phylloquinone (Vitamin K1, phyQ), 5-betacholestane-3-alpha (link), which is a bile acid synthesis pathway intermediate, and biotin (btn), which is a small vitamin molecule that acts as a cofactor in oxidative metabolism. The phenotypic perturbation pipeline predicted a set of exchange reactions that consistently vary as a result of knock-out of either the GBA1 gene, encoding

lysosomal and cytoplasmic glucocerebrosidase, or complete inhibition of mitochondrial complex 1 (Figure 5.3b).

Tracer-based metabolomic experimental design. A subset of the iNESC2DN model was atomically resolved using the COBRA Toolbox v3.0[16]. Specifically, a submodel was generated from the majority (1,091/1,533) internal reactions where a balanced atom mapping could be algorithmically predicted using the Reaction Decoder Tool[31], including manual correction of R-group specification in appropriate substrate-reactant pairs, not previously done for the atom mappings reported in Recon3D[8]. No balanced atom mappings could be computed for 442 reactions in the iNESC2DN model, as at least one molecular structure was not available for each reaction or the corresponding reaction was unbalanced. In the submodel, a total of 215 conserved moieties, their corresponding chemical structures and moiety subnetworks were identified. Using this subModel we predicted the non-trivial conserved moieties associated with all of the metabolites that could be taken up from the fresh medium, which therefore could be used in future tracer-based metabolomic experiments. For example, a conserved moiety, with molecular formula N4C4, is predicted to be taken up from the medium within hypoxanthine and is present in 90 different metabolites in the subModel including 5-Methylthioadenosine, AMP, ATP and hexanoyl coenzyme A, each of which have the potential to be secreted by the iNESC2DN model.

Discussion

Advances in constraint-based reconstruction and analysis. Completion of this study required several advances in constraint-based reconstruction and analysis. For example, this modelling approach is most commonly applied to biochemical systems where one predicts a feasible steady state flux vector that also satisfies a biologically motivated cellular objective, e.g., maximisation of biomass production flux for an exponentially growing culture of bacteria[26]. However, neither substantia nigra dopaminergic neurons nor differentiated dopaminergic neurons divide, and it is not known what the cellular objective is for such neurons. Therefore, we added new constraints that enforce certain internal reactions, or combinations thereof, to operate above a certain flux, e.g., constraints on the turnover rate for metabolites and constraints representing the energetic requirements for biomass maintenance and electrophysiological signalling. As no cellular objective is assumed, uniform

sampling[42] was applied, e.g., to reliably predict the sets of reaction fluxes that vary most in response to a PD relevant perturbation. This required the development and application of a novel algorithm, guaranteed to uniform sampling of the steady state solution space of high-dimensional metabolic networks[15], such as those derived from Recon3D.

Another example of a novel advance in constraint-based reconstruction and analysis is our pipeline (Figure 5.1) to generate a constraint-based metabolic model of a non-dividing cell that starts with the most comprehensive generic metabolic network to date, Recon3D[8], and integrates biochemical, transcriptomic, exometabolomic and manually curated data. It allows the generation of a variety of *in silico* models of neuronal metabolism, in a more comprehensive manner than previously described methods[23] and models[18]. The pipeline is sufficiently flexible that it can be used to generate context-specific, genome-scale metabolic models using data from dopaminergic neurons with different genetic backgrounds and different conditions, e.g., mitochondrial monogenic PD patient-derived cultures (e.g., PINK1) and isogenic control cultures exposed to mitochondrial stressors.

Biochemical interpretation of well predicted metabolic characteristics. Variants of the iNESC2DN model performed well at quantitatively predicting metabolite secretion fluxes, given quantitative bounds on metabolite uptake fluxes, and at quantitatively predicting metabolite uptake fluxes, given quantitative bounds on metabolite secretion fluxes (Figure 5.2). Of the analysis methods tested, uniform sampling of steady state fluxes yielded the best predictions of quantitative secretion fluxes, especially for proline, putrescine and asparagine. The iNESC2DN model predicts the potential to uptake or secrete many metabolites that are not constrained by our quantitative exometabolomic data. Of the unmeasured metabolites predicted to be secreted by the iNESC2DN model, at least 30 are specifically associated with neuronal disorders (Table S-3), e.g., increased pyroglutamic acid is an indicator of glutathione deficiency and is associated with brain toxicity due to formation of amino acid adducts and dopamine quinones[13].

All vulnerable neuronal populations in Parkinson's disease seem to either use monoamine neurotransmitters, such as dopamine (dopaminergic neurons within substantia nigra pars compacta), norepinephrine (noradrenergic neurons in locus coeruleus), and serotonin (serotonergic neurons in raphe nucleus), or produce

cytosolic monoamines, such as the cholinergic neurons of the dorsal motor nucleus of the vagus[36, 25]. Also, high levels of cytosolic monoamines are hypothesised to underlie selective degeneration, since vulnerable neuronal populations generally include a catecholamine-derived neuromelanin pigment[36, 44]. Consistent with phenylalanine being the precursor of monoamine neurotransmitters, the iNESC2DN model includes a high representation of reactions from the phenylalanine, tyrosine and tetrahydrobiopterin metabolism.

Most of the cellular phenotypic traits that are shared between vulnerable neuronal populations in Parkinson's disease, can be associated with a metabolic burden[36]. Such neurons require a high supply of energy in order to meet the demand to tonically propagate action potentials over a large axonal arbour and for the synthesis, release and reuptake of neurotransmitters[47, 36]. This intrinsic need to produce and consume a large amount of energy is thought to makes these neurons especially vulnerable to any impairment of energy metabolism[47, 45], therefore mitochondrial deficits could drive pathogenesis in Parkinson's disease[38, 37, 36]. Consistent with this, in the iNESC2DN model we observe an increased representation of reactions related with oxidative phosphorylation, mitochondrial transport and the metabolism of cofactors, such as NAD metabolism.

The predicted minimal medium, which is the minimum number of metabolites required to be taken up by the model, consists of typical energetic substrates, essential amino acids and certain nonessential amino acids. In particular, L-glutamine is a non-essential amino acid that can be converted into nucleotides that then serve as a source of energy. Recently, a novel link has been described between glycolysis and mitochondrial dysfunction, which is mediated by reductive carboxylation of L-glutamine[12]. A decrease in utilisation of reduced nicotinamide adenine dinucleotide (NADH) by the mitochondrial respiratory chain results in cytosolic reductive carboxylation of glutamine and thereby cytosol-confined NADH recycling. It is not known if this mechanism is of particular interest for PD. The minimal set of active reactions also predicted the activity of many reactions in dopamine metabolism, reflecting the importance of these reactions within the metabolic network. The set of minimal medium metabolites for an *in vitro* dopaminergic neuron provides a basis for the rational design of defined fresh medium specific for neuronal cell cultures[5].

Biochemical interpretation of poorly predicted metabolic characteristics. When disparate biochemical information from different experiments is integrated into a constraint-based model, they must be made consistent because inconsistent constraints will lead to an infeasible model, that is, one which does not admit any steady state flux. Therefore, it is important to achieve a balance between integration of further prior information, with the aim to improve quantitative predictions, and the risk of infeasibility due to inconsistency. As an example, the glutathione transferase (VMH link) reaction in dopamine metabolism was manually curated to be active since it is present in dopaminergic neurons[11], but it was excluded during model generation as it was not part of any flux consistent pathway in the generic Recon3D model. This indicates a metabolic pathway that requires future manual curation in the next iteration of the generic human metabolic reconstruction. Furthermore, qualitative metabolic predictions were made concerning secreted metabolites that may be important for dopaminergic neurons, but they were not tested because the targeted metabolomic platforms were initially chosen before the model existed.

Exometabolomic concentration changes for L-proline and serine, could not be directly integrated with the preconditioned model without making it inconsistent with the existence of a steady state flux. Recon3D allows reversible transport of the conditionally essential amino acid, L-proline. Prior to addition of exometabolomic data, the context-specific model includes extracellular transport reactions for L-proline, e.g., via proton symport PROT2r, but does not require secretion of L-proline, only either uptake or secretion is required. Therefore, when the exometabolomic data, which observes secretion of L-proline, is attempted to be integrated with the draft context-specific model, it may not be, and in this case is not feasible to obtain a steady state flux that secretes L-proline. Therefore, relaxation of the exometabolomic constraint, to permit L-proline uptake by the model, is required to render the model feasible. The situation is the same for serine, a non-essential amino acid. Essentially the common issue here is that data on the presence of gene products only provides information that the corresponding reaction may be active, but not the direction that the corresponding reaction is active in.

Relationship between *in vivo*, *in vitro* and *in silico*. Manual curation of the literature focused on quantification of neuronal molecular composition, turnover

fluxes, active genes, active reactions and inactive reactions specific to neurons, and substantia nigra dopaminergic neurons in particular. In parallel, we integrated transcriptomic and metabolomic data from human neuroepithelial stem cell derived neurons in macroscopic culture. As such, the iNESC2DN model is an *in silico* model that particularly emphasises the properties of human substantia nigra dopaminergic neurons and the properties of human neuroepithelial stem cell derived neurons[33]. The macroscopic culture is a state of the art *in vitro* model of a human substantia nigra dopaminergic neuron *in vivo*. However, a single DN emanating from the substantia nigra is characterised by a massive axonal arbour[21], much larger than other neuronal types, and projects to ~200k terminals in the striatum[29]. In contrast, the *in vitro* neurons do have extensive neuronal projections, but not to the same extent as *in vivo*. Like this morphological divergence, there may be a molecular divergence between the *in vivo* neuron, on which manual curation was based, and on the *in vitro* neuronal culture used for generation of transcriptomic and metabolomic data, which is not pure culture of DN and may have a different extracellular metabolome. It will be interesting to compare this version of the iNESC2DN model with future versions generated using protocols already in development for generation of higher purity dopaminergic neuronal cultures.

Exometabolomic experimental design. Algorithmic experimental design was used to propose designs that optimise the information obtained in future exometabolomic and tracer-based metabolomic experiments. Algorithmic design of exometabolomic experiments enables optimal selection and development of targeted mass spectrometry platforms for future analyses. This is important as one targeted analytical platform cannot quantify the concentration of all of the metabolites within the iNESC2DN model (supplementary information section S15). Our uncertainty reduction pipeline rank orders unmeasured exchanged metabolites by the degree to which their measurement would shrink the feasible set of steady-state flux vectors. The top ranked metabolites include biotin, which is known to be enriched in select areas of the central nervous system, including the substantia nigra[22]. Phylloquinone interacts with the N-terminus of alpha-synuclein, inhibits fibril formation in vitro and is being investigated with a view toward development of new therapies targeting alpha-synuclein aggregation[10].

Design of tracer-based metabolomic experiments. The pipeline for tracer-based metabolomic experiment design is hampered by the absence of molecular structures for some reactants[30], e.g., those with R groups in the structure, as they precluded the atomic resolution of all reactions in the iNESC2DN model. However, it was possible to atom map the majority of internal reactions, which permitted the identification of the majority of conserved moieties[14] in the iNESC2DN model. Identification of conserved moieties has strong potential for use in design of tracer-based metabolomic experiments[46]. By isotopically labelling any single atom in a conserved moiety, one can use the iNESC2DN model to predict the reachable set of metabolites that could contain that isotopic label, or any other isotopically labelled atom in the same conserved moiety. For a single conserved moiety, this approach for the design of an isotopic labelling strategy has been explored with the related concept of an elementary metabolic unit[2]. This will facilitate future study of metabolic pathways particularly significant for identified by our exometabolomic approach in more detail.

Conclusions

We have developed the first, mechanistic, genome-scale, metabolic model of a pluripotent stem cell derived dopaminergic neuronal culture, denoted iNESC2DN. It combines extensive manual curation of biochemical literature with genome-scale quantification of transcripts and extracellular metabolite concentration changes. The model also atomically resolves metabolic transformations at genome-scale. Variants of the model, tested against subsets of independent exometabolomic data, could quantitatively predict metabolite uptake and secretion fluxes for many fresh and spent medium metabolites. With a view towards future metabolomic experiments to refine the model in an iterative systems biology cycle, we demonstrate its utility for experimental design of targeted metabolomic and tracer-based metabolomic experiments. As such, the iNESC2DN model establishes a solid foundation for comparative analyses of neuroepithelial stem cell derived dopaminergic neurons from PD patients and controls via mechanistic model-driven metabolomic and tracer-based metabolomic approaches, and we expect, that this strategy will be very useful also for other neurodegenerative diseases.

Acknowledgements

The authors would like to thank Sylvain Arreckx and Thomas Pfau for helping with computational issues, Maike Aurich for helping with MetaboTools, Swagatika Sahoo explanation of the reconstruction process. ELM, MO, and DE were supported Aides à la Formation-Recherche Training allowances granted to by the Fonds National de la Recherche Luxembourg. ZZ and EG were supported by the Fonds Nationale de la Recherche, Luxembourg, as part of the BMBF-funded e:Med project MitoPD (INTER/BMBF/13/04) and the CORE INTER project MiRisk-PD (FNR11676395). LH has been supported by the FNR OPEN Grant (FNR/O16/11402054). The bioinformatic analyses presented in this paper were carried out in part using the HPC facilities of the University of Luxembourg (see http://hpc.uni.lu). The provision of NESC from the StemBANCC project is gratefully acknowledged. JM, ELM, GP, JS, CW, TH and RF received funding from the European Union's Horizon 2020 research and innovation programme, for the project SysMedPD, under grant agreement no. 668738.

References

1. Rodrigo D. A.M. Alves et al. “Global Profiling of theMuscleMetabolome:Method Optimization, Validation and Application to Determine Exercise-Induced Metabolic Effects”. In: *Metabolomics* 11.2 (Apr. 1, 2015), pp. 271–285. doi: 10.1007/s11306-014-0701-7.
2. Maciek R. Antoniewicz, Joanne K. Kelleher, and Gregory Stephanopoulos. “Elementary Metabolite Units (EMU): A Novel Framework for Modeling Isotopic Distributions”. In: *Metabolicengineering* 9.1 (Jan. 2007), pp. 68–86. doi: 10.1016/j.ymben.2006.09.001.
3. Maike K. Aurich, Ronan M. T. Fleming, and Ines Thiele. “MetaboTools: A Comprehensive Toolbox for Analysis of Genome-Scale Metabolic Models”. In: *Frontiers in Physiology* 7 (2016). doi: 10.3389/fphys.2016.00327.
4. Maike K. Aurich et al. “Prediction of Intracellular Metabolic States from Extracellular Metabolomic Data”. In: *Metabolomics* 11.3 (Aug. 14, 2014), pp. 603–619. doi: 10.1007/s11306-014-0721-3.
5. Cedric Bardy et al. “Neuronal Medium That Supports Basic Synaptic Functions and Activity of Human Neurons in Vitro”. In: *Proceedings of the National Academy of Sciences of the United States of America* 112.20 (May 19, 2015), E2725–E2734. doi: 10.1073/pnas.1504393112. pmid:25870293.
6. Milena Bellin et al. “Induced Pluripotent Stem Cells: The New Patient?” In: *Nature Reviews Molecular Cell Biology* 13.11 (Nov. 2012), pp. 713–726. doi: 10.1038/nrm3448.
7. J Paul Bolam and Eleftheria K Pissadaki. “Living on the Edge with Too Many Mouths to Feed: Why Dopamine Neurons Die”. In: *Movement Disorders* 27.12 (Sept. 2012), pp. 1478–1483. doi: 10.1002/mds.25135. pmid: 23008164.
8. Elizabeth Brunk et al. “Recon3D Enables a Three-Dimensional View of Gene Variation in Human Metabolism”. In: *Nature Biotechnology* 36 (Feb. 19, 2018), p. 272. url: http://dx.doi.org/10.1038/nbt.4072.
9. Sriram Chandrasekaran et al. “Comprehensive Mapping of Pluripotent Stem Cell Metabolism Using Dynamic Genome-Scale Network Modeling”. In: *Cell Reports* 21.10 (Dec. 5, 2017),pp. 2965–2977. doi: 10.1016/j.celrep.2017.07.048. pmid: 29212039.

10. Fernanda Luna da Silva et al. “Vitamins K Interact with N-Terminus - Synuclein and Modulate the Protein Fibrillization in Vitro. Exploring the Interaction between Quinones and alpha-Synuclein”. In: *Neurochemistry International* 62.1 (Jan. 1, 2013), pp. 103–112. doi: 10.1016/j.neuint.2012.10.001.
11. Alexies Dagnino-Subiabre et al. “Glutathione TransferaseM2-2 Catalyzes Conjugation of Dopamine and Dopa o-Quinones”. In: *Biochemical and Biophysical Research Communications* 274.1(July 21, 2000), pp. 32–36. doi: 10.1006/bbrc.2000.3087.
12. Edoardo Gaude et al. “NADH Shuttling Couples Cytosolic Reductive Carboxylation of Glutamine with Glycolysis in Cells with Mitochondrial Dysfunction”. In: *Molecular Cell* 69.4 (Feb. 15,2018), 581–593.e7. doi: 10.1016/j.molcel.2018.01.034. pmid: 29452638,29452638.
13. Greenblatt, James M. and Brogan, Kelly. *Integrative Therapies for Depression: Redefining Models for Assessment, Treatment and Prevention*. Dec. 1, 2015. url: https://w/ww.crcpress.com / Integrative - Therapies - for - Depression - Redefining - Models - for - Assessment /Greenblatt-Brogan/p/book/9781498702294 (visited on 02/01/2018).
14. Hulda S. Haraldsdóttir and Ronan M. T. Fleming. “Identification of Conserved Moieties in Metabolic Networks by Graph Theoretical Analysis of Atom Transition Networks”. In: *PLOS Computational Biology* 12.11 (Nov. 21, 2016), e1004999. doi: 10.1371/journal.pcbi.1004999.
15. Hulda S. Haraldsdóttir et al. “CHRR: Coordinate Hit-and-Run with Rounding for Uniform Sampling of Constraint-Based Models”. In: *Bioinformatics* 33.11 (Jan. 6, 2017), pp. 1741–1743. doi: 10.1093/bioinformatics/btx052.
16. Laurent Heirendt et al. “Creation and Analysis of Biochemical Constraint-Based Models: The COBRA Toolbox v3.0”. In: *Nature Protocols (accepted)* (2018). url: https://arxiv.org/abs/1710.04038 (visited on 07/28/2017).
17. Ji-feng Kang, Bei-sha Tang, and Ji-feng Guo. “The Progress of Induced Pluripotent Stem Cells as Models of Parkinson’s Disease”. In: *Stem Cells International* 2016 (2016). doi: 10.1155/2016/4126214. pmid: 26880962.
18. Nathan E Lewis et al. “Large-Scale in Silico Modeling of Metabolic Interactions between Cell Types in the Human Brain”. In: *Nature Biotechnology* 28.12 (Dec. 2010), pp. 1279–1285. doi:10.1038/nbt.1711.

19. E. Lucumi Moreno et al. “Differentiation of Neuroepithelial Stem Cells into Functional Dopaminergic Neurons in 3D Microfluidic Cell Culture”. In: *Lab on a Chip* 15.11 (May 20, 2015),pp. 2419–2428. doi: 10.1039/C5LC00180C.
20. R. Mahadevan and C. H. Schilling. “The Effects of Alternate Optimal Solutions in Constraint-Based Genome-Scale Metabolic Models”. In: *Metabolic Engineering* 5.4 (Oct. 2003), pp. 264–276. doi: 10.1016/j.ymben.2003.09.002.
21. Wakoto Matsuda et al. “Single Nigrostriatal Dopaminergic Neurons Form Widely Spread and Highly Dense Axonal Arborizations in the Neostriatum”. In: *The Journal of Neuroscience* 29.2 (Jan. 14, 2009), pp. 444–453. doi: 10.1523/JNEUROSCI.4029-08.2009. pmid: 19144844.
22. Bruce E. McKay, Michael L. Molineux, and Ray W. Turner. “Biotin Is Endogenously Expressed in Select Regions of the Rat Central Nervous System”. In: *The Journal of Comparative Neurology* 473.1 (May 17, 2004), pp. 86–96. doi: 10.1002/cne.20109.
23. Monica L. Mo, Bernhard Ø Palsson, and Markus J. Herrgård. “Connecting Extracellular Metabolomic Measurements to Intracellular Flux States in Yeast”. In: *BMC Systems Biology* 3.1 (Mar. 25, 2009), p. 37. doi: 10.1186/1752-0509-3-37. pmid: 19321003.
24. Marek J. Noga et al. “Metabolomics of Cerebrospinal Fluid Reveals Changes in the Central Nervous System Metabolism in a Rat Model of Multiple Sclerosis”. In: *Metabolomics* 8.2 (Apr. 2011), pp. 253–263. doi: 10.1007/s11306-011-0306-3.
25. Miguel A. P. Oliveira et al. “Embryonic Development of Selectively Vulnerable Neurons in Parkinson’s Disease”. In: *npj Parkinson’s Disease* 3.1 (June 26, 2017), p. 21. doi: 10.1038/s41531-017-0022-4.
26. Jeffrey D. Orth, Ines Thiele, and Bernhard Ø Palsson. “What Is Flux Balance Analysis?” In: *Nature Biotechnology* 28.3 (Mar. 2010), pp. 245–248. doi: 10.1038/nbt.1614.
27. G. Paglia et al. “Monitoring Metabolites Consumption and Secretion in Cultured Cells Using Ultra-Performance Liquid Chromatography Quadrupole-Time of Flight Mass Spectrometry (UPLC-Q-ToF-MS).” In: *Analytical and Bioanalytical Chemistry* 402.3 (2012), pp. 1183–98. doi:10.1007/s00216-011-5556-4. pmid: 22159369.

28. Bernhard Ø Palsson. *Systems Biology: Constraint-Based Reconstruction and Analysis*. Cambridge, England: Cambridge University Press, Jan. 26, 2015. 550 pp.
29. Eleftheria K. Pissadaki and J. Paul Bolam. "The Energy Cost of Action Potential Propagation in Dopamine Neurons: Clues to Susceptibility in Parkinson's Disease". In: *Frontiers in Computational Neuroscience* 7 (Mar. 18, 2013), p. 13. doi: 10.3389/fncom.2013.00013. pmid:23515615.
30. German A. Preciat Gonzalez et al. "Comparative Evaluation of Atom Mapping Algorithms for Balanced Metabolic Reactions: Application to Recon3D". In: *Journal of Cheminformatics* 9 (2017), p. 39. doi: 10.1186/s13321-017-0223-1.
31. Syed Asad Rahman et al. "Reaction Decoder Tool (RDT): Extracting Features from Chemical Reactions". In: *Bioinformatics* 32.13 (Jan. 7, 2016), pp. 2065–2066. doi: 10.1093/bioinformatics/btw096. pmid: 27153692.
32. Rawi Ramautar et al. "Human Metabolomics: Strategies to Understand Biology". In: *Current Opinion in Chemical Biology*. In Vivo Chemistry • Analytical Techniques 17.5 (Oct. 2013), pp. 841–846. doi: 10.1016/j.cbpa.2013.06.015.
33. Peter Reinhardt et al. "Derivation and Expansion Using Only Small Molecules of Human Neural Progenitors for Neurodegenerative Disease Modeling". In: *PLoS ONE* 8.3 (Mar. 22, 2013). Ed. By Marcel Daadi, e59252. doi: 10.1371/journal.pone.0059252.
34. Kirti Sharma et al. "Cell Type- and Brain Region-Resolved Mouse Brain Proteome". In: *Nature Neuroscience* advance online publication (Nov. 2, 2015). doi: 10.1038/nn.4160.
35. P. A. Steininger et al. "Change of the Metabolomic Profile during Short-Term Mononuclear Cell Storage". In: *Vox Sanguinis* (Jan. 1, 2017), n/a–n/a. doi: 10.1111/vox.12482.
36. David Sulzer and D. James Surmeier. "Neuronal Vulnerability, Pathogenesis and Parkinson's Disease". In: *Movement disorders : official journal of the Movement Disorder Society* 28.1 (Jan. 2013), pp. 41–50. doi: 10.1002/mds.25095. pmid: 22791686.

37. D. James Surmeier, José A. Obeso, and Glenda M. Halliday. “Selective Neuronal Vulnerability in Parkinson Disease”. In: *Nature Reviews Neuroscience* 18.2 (Jan. 20, 2017), pp. 101–113. doi:10.1038/nrn.2016.178.
38. D. James Surmeier and David Sulzer. “The Pathology Roadmap in Parkinson Disease”. In: *Prion* 7.1 (Jan. 1, 2013), pp. 85–91. doi: 10.4161/pri.23582.
39. Kazutoshi Takahashi et al. “Induction of Pluripotent Stem Cells from Adult Human Fibroblasts by Defined Factors”. In: *Cell* 131.5 (Nov. 30, 2007), pp. 861–872. doi: 10.1016/j.cell.2007. 11.019.
40. Ines Thiele and Bernhard Ø Palsson. “A Protocol for Generating a High-Quality Genome-Scale Metabolic Reconstruction”. In: *Nature Protocols* 5.1 (Jan. 2010), pp. 93–121. doi: 10.1038/nprot.2009.203.
41. Ines Thiele et al. “A Community-Driven Global Reconstruction of Human Metabolism”. In: *Nature Biotechnology* 31.5 (May 2013), pp. 419–425. doi: 10.1038/nbt.2488.
42. Ines Thiele et al. “Candidate Metabolic Network States in Human Mitochondria. Impact of Diabetes, Ischemia, and Diet.” In: *Journal of Biological Chemistry* 280.12 (Mar. 25, 2005), pp. 11683–11695. doi: 10.1074/jbc.M409072200.
43. Nikos Vlassis, Maria Pires Pacheco, and Thomas Sauter. “Fast Reconstruction of Compact Context-Specific Metabolic Network Models”. In: *PLoS Comput Biol* 10.1 (Jan. 16, 2014), e1003424. doi: 10.1371/journal.pcbi.1003424.
44. Eberhard Weihe et al. “Three Types of Tyrosine Hydroxylase-Positive CNS Neurons Distinguished by Dopa Decarboxylase and VMAT2 Co-Expression”. In: *Cellular and molecular neurobiology* 26.0 (2006), pp. 659–678. doi: 10.1007/s10571-006-9053-9. pmid: 16741673.
45. Peter Wellstead and Mathieu Cloutier. “An Energy Systems Approach to Parkinson’s Disease”.In: *Wiley Interdisciplinary Reviews: Systems Biology and Medicine* 3.1 (Jan. 1, 2011), pp. 1–6. doi: 10.1002/wsbm.107.
46. Wolfgang Wiechert. “13C Metabolic Flux Analysis”. In: *Metabolic Engineering* 3.3 (July 2001), pp. 195–206. doi: 10.1006/mben.2001.0187.
47. Weihai Ying. “NAD+ and NADH in Brain Functions, Brain Diseases and Brain Aging”. In: *Frontiers in Bioscience: A Journal and Virtual Library* 12 (2007), pp. 1863–1888. pmid: 17127427.

5

Supporting Information

Part I

Methods

S1 Experiments

S1.1 Cell culture

An overview of the experimental approach is given in Figure S4.

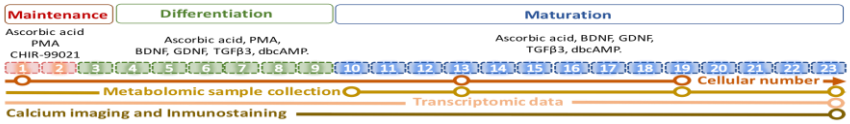

Figure S4: Experimental protocol overview.

Human neuroepithelial stem cells (hNESC) were differentiated into midbrain dopaminergic neurons. The cell number in each culture well was counted on day 1, 13, 19 and estimated for day 23. Spent media samples for metabolomic analyses were collected at days 10, 13, 19 and 23. Samples were analysed with both GC-MS and LC-MS. At day 23, live cells were subjected to calcium imaging followed by immunostaining assays, and collection of parallel samples for transcriptomic analysis. The media composition at the various stages of cell culture were as follows; Maintenance stage (red): maintenance medium containing ascorbic acid, purmorphamine (PMA) and the aminopyrimidine CHIR-99021(CHIR). Differentiation stage (green): differentiation medium containing ascorbic acid, Brain-derived neurotrophic factor (BDNF), glial cell-derived neurotrophic factor (GDNF), Transforming Growth Factor Beta 3 (TGFβ3), dbcAMP and PMA. Maturation stage (blue): differentiation media without PMA.

S1.1.1 Human neuroepithelial stem cell-derived dopaminergic neuronal differentiation.

A human neuroepithelial stem cell line from a healthy human donor (Identifier: 3.0.0.10.0 Acronym: hNESCs K7/ NPBSCs/NEs, wild-type) was maintained and differentiated into DNs, using an established protocol[54], summarised below.

N2B27 Medium preparation. The culture medium, denoted *N2B27 medium,* was used as the basis to prepare both maintenance and differentiation media and was

obtained by mixing equal amounts of Neurobasal medium (Invitrogen/Life Technologies) and DMEM/F12 medium (Invitrogen/Life Technologies) supplemented with 1% penicillin and streptomycin (Life Technologies), 2 mM L-glutamine (Life Technologies), 0.5 X B27 supplement without Vitamin A (Life Technologies) and 0.5 X N2 supplement (Life Technologies). The final concentration of the media composition is fully detailed in Table S-4.

Plate coating. Nunc cell-culture treated 6-well plates (ThermoFisher scientific, Roskilde, Denmark) were coated with 1% Matrigel (Discovery Labware, Inc., Two Oak Park, Bedford, MA, USA, Catalogue number 354277, lot number 3318549) in 600 µ L of knockout DMEM (1X) medium.

Cell seeding and maintenance. At the time of cell seeding, the knockout DMEM (1X) medium from the coating step, was removed from each well and the K7 hNESC line was seeded in three replicate wells. The medium to maintain the hNESC in culture, denoted *maintenance medium* (red in Figure S4: Overview of the experimental protocol), is based on N2B27 medium with 0.5 μM PMA (Enzo life sciences), 3 μM CHIR (Axon Medchem) and 150 μM ascorbic acid (Sigma Aldrich). The cell seeding was done by preparing 5 × 10^6 million cells/mL in 50% matrigel in maintenance medium and adding 200 μL of this preparation to obtain approximately 0.2 mm or 200 μm thick layer of cells in three dimensions within Matrigel, with 4 × 10^5cells per well. After the Matrigel and cell mixture was added to the well, the plate was incubated for 2 min at 37 °C to gelate the matrigel layer, the plate was then taken out of the incubator and 2.8 mL of maintenance medium was added and the plate was incubated at 37 °C and 5% CO_2 for 48 h.

Neuronal differentiation and maturation. The *differentiation medium with PMA* preparation to induce the differentiation of hNESC towards midbrain dopaminergic neurons consisted of N2B27 medium with 200 µ M ascorbic acid, 0.01 ng/ µ L BDNF (Peprotech), 0.01 ng/ µ L GDNF (Peprotech), 0.001 ng/ µ L TGF β 3 (Peprotech), 2.5 µ M dbcAMP (Sigma Aldrich) and 1 µ M PMA. This medium preparation was completely replaced every 2 days during the next 6 days of culture in the differentiation process. For the maturation of differentiated neurons, PMA is required to be absent from the differentiation medium. This *differentiation medium*

without PMA was used from day 9 onwards and 50% media replacement every 2 days for 3 weeks.

S.1.1.2 Microscopy and calcium imaging

To monitor cellular morphology during differentiation, bright field images were acquired every 48h for 23 days of differentiation using a Zeiss Axiovert 40 CFL microscope equipped with a cooled charge-coupled device based camera (Zeiss AxioCam MRm, Zeiss). At day 23 in culture, calcium imaging was done with a Fluo-4 AM green-fluorescent calcium indicator dye. After removing the differentiation medium, 1 mL of 5μM cell permeant Fluo-4 AM (Invitrogen/Life Technologies, F14201) in neurobasal medium, was added to selected wells of a 6-well plate at room temperature. Full frame fluorescence images, of size 2560×2160 pixels, were acquired using an epifluorescence microscope (Leica DMI6000 B, Germany) equipped with a cooled sCMOS camera (Neo 5.5, Andor technology, UK) and both were controlled with Micro-manager (version 1.4)[13]. Images were sampled at a rate of approximately 10 Hz for about 2 min, stored as image stacks and analysed off-line using MATLAB (release 2013b; Mathworks). To automatically detect the neurons, we used the ADINA toolbox[12] (https://bitbucket.org/jakirkham/adina-toolbox-v0.1/src), which is a set of MATLAB functions specifically developed for the analysis of calcium imaging data. This includes a segmentation step where regions of interest corresponding to individual neurons are selected. For each segmented neuron, we measured fluorescence traces as relative changes in fluorescence intensity over time.

S1.1.3 Immunofluorescence staining assay

Immunostaining for a dopaminergic marker, tyrosine hydroxylase (TH) and a pan neuronal marker, Class III β-tubulin (TUBbIII) were used to identify differentiated dopaminergic neurons. Immunostaining for tyrosine hydroxylase (TH) positive differentiated neurons was performed on wells of a 6-well plate after day 25 of differentiation. Differentiated cells were fixed with 4 % PFA in 1× phosphate-buffered saline (PBS) (15 min), followed by permeabilisation with 0.05% Triton-X 100 in 1× PBS (3 min on ice), and blocking with 10% fetal calf serum (FCS) in 1× PBS (1 h). After washing with 1× PBS, the primary antibodies mouse anti-TUBβIII (1:1000, Covance, Germany), rabbit anti TH (1:1000, Santa Cruz biotechnology, Germany) and chicken anti-GFAP (1:1000, Merck Millipore, Germany), were

incubated for 90 min at 25 °C. After washing with 1× PBS, the secondary antibodies Alexa Fluor 488 Goat Anti-Rabbit (1:1000, Invitrogen), Alexa Fluor 568 Goat Anti-Mouse (1:1000, Invitrogen), Alexa Fluor 647 Goat Anti-chicken (1:1000, Invitrogen) and Hoechst 33342 to stain DNA (1:10000, Invitrogen), were incubated overnight at 4 °C. After washing with 1× PBS, confocal images of areas of selected wells were acquired, using a confocal microscope (Zeiss LSM 710).

S1.2 Transcriptomic analyses

S1.2.1 Cell culture

A human neuroepithelial stem cell line from a healthy donor was maintained and differentiated into DNs, using an established protocol[54], described in supplementary information section S1.1.1, with the following adaptions. The hNESCs were cultivated in mTESR1 medium (StemCell technologies, #05850) on 6-well dishes coated with Matrigel (Corning, #354263). The media composition, to the extent that it has been defined by the manufacturer, is detailed in Table S-4. At 23 days of the protocol (Figure S4), the percentage of TH positive cell was estimated between 15-20%. Since protein content per cell can vary from 2.46×10^{-5} to $4.71 \times 10^{-5} \mu g$/cell, protein content was measured using a Bradford protein assay.

S1.2.2 RNA preparation

RNA extraction The Ambion Magmax™-96 total RNA isolation kit (Life Sciences) was used for RNA extraction. Magnetic beads were used to isolate nucleic acids. Afterwards, the samples were washed and purified with DNAase. The RNA obtained was eluted in $50 \mu M$ elution buffer. Fragment Analyzer (Aligent Technologies Inc.) was used to measure RNA quality and concentration.

RNA-sequencing protocol RNA-sequencing data was generate from a hNESC-derived dopaminergic neuronal cell culture at day 23 in culture. The sequencing library preparation was done using 200 ng of total RNA input with the TrueSeq RNA Sample Prep Kit v3-Set B (RS-122-2002, Illumina Inc, San Diego, CA) producing a 275 bp fragment including adapters in average size. In the final step before sequencing, twelve individual libraries were normalised and pooled together using the adapter indices supplied by the manufacturer. Pooled libraries have then been clustered on

the cBot Instrument (Illumina Inc, San Diego, CA) using the TruSeq SR Cluster Kit v3-cBot-HS (GD-401-3001, Illumina Inc, San Diego, CA) sequencing was then performed as 78 bp, single reads and 7 bases index read on an Illumina HiSeq3000 instrument using the TruSeq SBS Kit HS- v3 (50-cycle) (FC-401-3002, Illumina Inc, San Diego, CA).

S1.3 Analysis of RNA sequencing data

The raw RNA-seq data were analysed with a custom-made RNA-seq analysis pipeline, which included publicly available software (SAMtools, version 0.1.18; FASTX-Toolkit, version 0.0.14)[36] and custom-made python scripts. The RNA-seq analysis pipeline consists of six main steps: (i) quality control for the raw RNA-seq reads; (ii) prepossessing of the raw RNA-seq reads to remove adapters and low-quality sequences; (iii) alignment of the reads to the human reference genome; (iv) assembly of the alignments into transcripts and (v) quantification of the expression levels of each gene. Briefly, the raw RNA-seq reads (length 52 nucleotides, single-end) of each sample were checked by FastQC (version 0.11.2) to determine the read quality. Adapter sequences and low quality sequences were removed by cutadapt (version 1.10)[39] using default settings. Reads with length less than 25 nucleotides were excluded from further analysis. Next, the alignment of RNA- seq reads against the human reference genome (NCBI build37.2, downloaded from iGenome of Illumina, https://support.illumina.com/sequencing/sequencing_software/igenome.html) was performed using TopHat2 (version 2.0.13)[30]. Alignment results were processed by Cufflinks (version 2.2.1)[67] for assembly of transcripts with default parameter settings. The quantification of gene expression was estimated by normalised FPKM (Fragments per kilobase of transcript per Million mapped reads) and counts at gene level by cuffnorm (version 2.2.1)[67]. In order to obtain one expression value per gene, we used the transcript with the largest average expression as representative for the corresponding gene, since measurements for low-abundance transcripts are less reliable. In case of replicated genes, the maximum value expression from replicates was averaged.

S1.4 Exometabolomic data

Table S-3 contains a list of target metabolites analysed with both LC-MS and GC-MS platforms: 75 biogenic amines and amino acids, and 24 organic acids. Aspartic acid is targeted in both platforms, therefore a total of 98 metabolites were targeted.

S1.4.1 LC-MS profiling of biogenic amines and amino acids

The analysis of 75 biogenic amines (Table S-3) was performed with an established LC-MS method[46]. Briefly, 15 μL of culture medium was extracted by adding 400 μL of ice-cold methanol, 55 μL of ice-cold milliQ water, 10 μL of tris(2-carboxyethyl)phosphine (TCEP; 1μg/μL) and 10 μL of a mixture of stable isotope labelled internal standards (Table S-3). The samples were vortexed for 10-20 seconds and centrifuged at 16000×g and 4 °C for 10 min. For the the calibration samples, 80 μL of each calibrant sample was mixed with 10 μL of TCEP (1 μg/μL) and 10 μL of internal standard mix and extracted with 400 μL of ice-cold methanol as for medium samples. After centrifugation, all supernatants were transferred into 1.5 mL tubes and the liquid extracts were evaporated in a vacuum concentrator (Labconco, Kansas City, MO, USA) to dryness. The dried extracts were first dissolved in 80 μL borate buffer (pH 9) and mixed with 20 μL of pure acetonitrile containing 3 μg/μL AccQ-Tag derivatisation reagent (Waters, Etten-Leur, Netherlands) to start the chemical derivatisation of the primary and/or secondary amine groups. The derivatisation reaction was performed at 55 °C for 30 min in a temperature-controlled orbital shaker (VWR Incubating Microplate Shaker, Germany). After completion of derivatisation, the samples were centrifuged at 16000×g and 4 °C for 2 min and 80 μL of the supernatant was transferred into LC vials for sample injection. 1 μL of the liquid extract was injected onto the analytical column for the analysis.

All measurements were performed with a Waters Acquity ultra-high pressure liquid chromatography (UPLC) (Milford, MA, USA) hyphenated with Agilent 6460 triple-quadrupole mass spectrometer (Palo Alto, CA, USA). Chromatographic separation was achieved on a Water Acquity HSS T3 C18 UPLC column (2.1×100 mm, 1.7 μm) and the metabolites were identified based on their retention time and via multiple reaction monitoring (MRM) transitions from their protonated precursor ions of the AccQ-Tag derivates into common product ion of 171 m/z with corresponding linear ranges and LOD values (Table S-3). The peak detection and integration were performed with Agilent MassHunter Quantitative Software v7.0 (Palo Alto, CA, USA).

For the concentration determination, the calibration lines were drawn on a concentration range over three orders of magnitude (0.1 μM - 100 μM). The calibrant and internal standards were spiked into blank solvent (methanol/water, 80%/20%; v/v) in which the area ratio of each target analyte to its corresponding internal standard was used to define the ordinate values of the calibration curve. In total, sixteen calibration points were selected where each six calibration point covers one order of magnitude (e.g. 100 nM - 1 μM: 100 nM, 200 nM, 400 nM, 600 nM, 800 nM, 1 μM). After linear regression, the linear response range for each metabolite was determined by Pearson's correlation coefficient ($R^2 \geq 0.95$) except dopamine and levodopa. The linear equation for each calibration line was used to convert area ratios obtained in samples into absolute quantities (in μM) by using a Macro formula in Microsoft Office 2010.

S1.4.2 GC-MS profiling of polar metabolites

Twenty-four polar metabolites (Table S-3) were analysed in culture media using a modified version of an in-house built GC-MS platform[3]. Because of the high abundance of D-glucose and L-lactic acid in culture media, samples were diluted 1:299 (v/v) in milliQ water. Fifty microliters of both diluted and non-diluted culture medium was extracted with 425 μL of an extraction solvent (methanol/water, 94%/6%; volume/volume) containing stable isotope labelled internal standards (Table S-3). After vortexing the samples for 10 min on a multivortex, the samples were centrifuged at 16000×g and 4 °C for 10 min. Four hundred microliters of the supernatant was transferred into a 1.5 mL tube and the solvent was evaporated in a vacuum concentrator (Labconco, Kansas City, MO, USA). Dry samples were resuspended for the oximation reaction in 35 μL of pyridine containing methoxyamine hydrochloride (15 μg/μL) and kept at 30 °C for 90 min. After the oximation of the aldehyde groups on reducing sugars and organic acids, samples were further derivatised with silylation reaction for 60 min in an orbital shaker (VWR, Germany). This reaction was carried out by adding 40 μL of MSTFA (N-methyl-N-trimethylsilylacetamide) into the samples. Subsequently, samples were centrifuged at 16000×g and room temperature for 5 min and 70 μL of the supernatant was transferred into silanized glass inserts. The GC-MS measurements were performed on an Agilent 7890A GC System coupled to a single 759 quadruple

5975C Mass Selective Detector. One microliter of sample was injected with splitless injection. The analytes were separated on an Agilent HP-5MS Ultra Inert capillary GC column (30 m, 250 μm ID, 0.25 μm film thickness). Metabolite identification was carried out by using the retention time of the chemical standards and mass spectral similarity of the fragmentation pattern with NIST MS Search Software (v2.0). The metabolite quantification was performed based on the specific fragment ion for each polar metabolite (Table S-3). Both peak extraction and integration were performed by using the vendor's software (Agilent MassHunter Quantitative software v5.0). The concentrations were determined by spiking eleven (for diluted samples) or six (for non-diluted samples) different concentration values of the chemical standards on a 50 μL of diluted (300x) or non-diluted mixture of study samples (e.g. quality control sample). The area ratio of each target analyte to its corresponding internal standard was used to measure the ordinate values for the calibration lines. After linear regression, the linear response range for each metabolite was determined by Pearson's correlation coefficient ($R^2 \geq 0.95$) except alpha-ketoglutaric acid. The concentration values are then calculated using Macro formula in Microsoft Office 2010.

S2 Reconstruction

S2.1 Active and inactive genes and reactions

A *context-specific metabolic model* contains only the set of reactions active in a particular context. Therefore, we assembled a core set of genes and metabolic reactions known to be active or inactive in dopaminergic neurons *in vivo* or in hNESC-derived dopaminergic neurons in culture. A core set of active genes (Table S-1), as well as active and inactive reactions (Table S-2) was obtained either from manual curation of the literature or from transcriptomic data. Manual curation, described below, was focused on the physiological and biochemical literature on dopamine metabolism, dopaminergic neuronal transporters, central carbon metabolism, mitochondria-associated reactions and genes. In addition, manual curation of the literature was used to determine the need for addition or deletion of external reactions that are required for modelling non-equilibrium steady-state fluxes in dopaminergic neuronal metabolism. The list of genes, established by manual curation to be metabolically active, was combined with the aforementioned

transcriptomic data and used to generate the context-specific model through gene-protein-reaction associations[64].

S2.2 Dopamine metabolism

A key characteristic of dopaminergic neurons is their ability to synthesise, degrade and release dopamine. Therefore, manual reconstruction of dopamine metabolism was emphasised. In Recon2[65], there were already 75 tyrosine related reactions distributed in 6 subsystems. This content was extended with information from a comprehensive literature review of dopamine metabolism[41] and additional manual curation of the literature (Table S-2), according to an established protocol[64].

S2.3 Dopaminergic neuronal transporters

The metabolic identity of a cell is strongly influenced by its ability to transport particular metabolites across its extracellular membrane, and in the metabolic model, this is represented by constraints on the corresponding exchange reactions, which define the boundary conditions of the model. To start the reconstruction of dopaminergic neuronal transporters, we began with the 1550 extracellular transport reactions in Recon 2.04[47], which correspond to 255 genes as identified by gene-protein reaction associations. Almost half (120/255) of the genes associated with extracellular transport reactions were manually curated. Manual curation of the experimental literature primarily involved the identification of transporters present in human substantia nigra pars compacta tissue or cell cultures of dopaminergic neurons through *in situ* hybridisation, RT-PCR, immunohistochemistry or immunoblotting. When human data was not found, data from rat or mouse was included instead. Additionally, when data specific for dopaminergic neurons or substantia nigra pars compacta was not found, evidence for transporters being present in neurons in general, astrocytes or blood brain barrier was used instead. After a review of metabolic genes active in the brain, only the genes specific for dopaminergic neurons or substantia nigra pars compacta were included in the list of active genes.

S3 Constraint generation

S3.1 Biomass maintenance and turnover constraints

Stoichiometric specification of biomass composition[15], as well as cellular synthesis and turnover requirements is an essential component for the specification of the objective function in constraint-based modelling. However, fully differentiated dopaminergic neurons do not replicate and therefore, it is sufficient if lipid, nucleic acid, and amino acid synthesis meet the demand for their turnover. Therefore, we adapted an established methodology[64] to define the minimal biomass maintenance and turnover requirements for dopaminergic neurons. This required manual curation of the neurochemical literature to extract biomass precursor turnover rates, fractional biomass composition, and identification of key degradation reactions for dopaminergic neurons. Where human data was not obtained, rodent data was used. Where human substantia nigra pars compacta dopaminergic neuronal data was not obtained, other neuronal data was used.

Biomass composition. TheRecon3D[7] biomass maintenance reaction was decomposed into its constituent biomass precursors. The fractional composition of a human substantia nigra pars compacta dopaminergic neuron was obtained by following several steps. First, the lipid and water fractional composition of a human substantia nigra pars compacta dopaminergic neuron was assumed to be the same as the one from a 55 year human cerebral cortex grey matter (39.6% dry weight of lipids and 60.4% dry weight of non-lipid residues and 82.3% wet weight water content)[49]. Furthermore, we used the protein wet weight (w/w) fractional composition for human substantia nigra (99 mg/g w/w)[5] to calculate the protein dry weight (DW) fractional composition. RNA and DNA dry weight fractional compositions for human substantia nigra (grey matter) were readily available in the literature (3,29 µg/mg DW of RNA and 1,81 µg/mg DW of DNA)[35]. Based on the relative concentrations of the different neuronal lipids, amino acids, and nucleic acids, the overall dry weight (DW) fractional human neural tissue composition was estimated to be 39.60% lipid, 55.93% protein, 0.18% DNA, 0.33% RNA, and 3.96% others[48].

The fractional composition (%) of each biomass precursor was converted into a reaction rate (μmol/gDW/h that is micromole per gram dry weight per hour). These values were then converted into fluxes (μmol/gDW/h) taking in consideration an

experimental time of 48h and a value for the dry weight of an hNESC-derived neuron ($DW(DN)$, gDW/cell). The latter was calculated using

$$DW(DN) \coloneqq \text{Protein content / protein percentage}$$

where the protein content (μg/cell) was obtained from the results of the aforementioned Bradford assay (0.0002459 to 0.00047053 μg/cell) and the protein percentage was based on the calculated fractional protein composition of a human substantia nigra pars compacta dopaminergic neuron. This is a coarse-grained approximation of neuronal lipid, amino acid, and nucleic acid maintenance requirements converted into μmol/gDW/h. The protein content ranged from 0.0002459 to 0.00047053 μg/cell. The protein percentage obtained from the literature is 55.93% protein[48]. Therefore, the dry weight of a single dopaminergic neuronal cell was estimated to be 6.4×10^{-10} gDW/cell, with a range of $4.4 - 8.41 \times 10^{-10}$.

Key degradation reactions. Using the neurochemical literature, the degradation pathway, or pathways, for each biomass precursor were identified and the first reaction in each degradation pathways was identified in Recon3D. For example, as reviewed in[31], phosphatidylserine is exclusively localised in the cytoplasmic leaflet of neuronal and astrocytic membranes, forming protein docking sites for signalling pathways. The phosphatidylserine decarboxylase enzyme is able to decarboxylate the serine moiety of phosphatidylserine to form phosphatidylethanolamine. Although one of the fatty acyl groups of phosphatidylserine can also be hydrolysed to convert phosphatidylserine into lysophosphatidylserine, this is quantitatively a minor pathway.

Turnover rates

The turnover rate of a metabolite reflects the rate at which that metabolite is replaced in a tissue, given by the reciprocal of the turnover time[40]. Turnover rates are commonly expressed as half-lives and represent the time, expressed in hours, required for half of the precursor to be replaced[33]. Metabolite half-lives $t_{1/2}$ were collected from the literature[33] and converted into turnover rates λ with

$$\lambda \coloneqq \ln(2) \,/\, t1/2 \qquad (1)$$

and then interpreted as constraints on degradation reaction rates. Turnover rates were converted to the same unit (μmol/gDW/h) as reaction rate, and applied as constraints, as described in supplementary information section S4.3.

S3.2 Maximum metabolite uptake constraints

Only the constituents of the defined fresh medium, plus some reversible extracellular transport reactions including water, carbon dioxide and oxygen, were permitted to be taken up by the model. That is, lower bounds on the corresponding exchange reactions were set by assuming that the maximum uptake rate is equal to the metabolite concentration in the fresh medium, divided by the duration of the interval being modelled (Table S-3). This is always an overestimate of the actual metabolite uptake rate, because it effectively assumes that the concentration of each uptaken metabolite is zero at the end of the time interval.

S3.3 Exometabolomically derived exchange reaction rate ranges

For each pair of quantitative measurements for the same metabolite at two time points, an exometabolomically derived exchange reaction rate, v_{exp}, was estimated for the corresponding metabolite by assuming a constant rate of change of metabolite concentration with respect to time and setting this rate of change of metabolite concentration to be equal to the experimentally measured flux when scaled appropriately with respect to the calculated dry cell mass in culture. The total dry weight for the *in vitro* cell culture (at day 19 and 23) was estimated from the product of the dry weight of a single neuron in culture times the number of cells in the cellular culture.

Cell number. The cell number in each culture well was measured on days 1, 13, 19, but not day 21 or 23 in culture. Therefore, the evolution of cell number with respect to time was estimated using a cubic spline fit to the measured cell numbers (Figure S5). Exometabolomic data was collected at day 9, 13, 19 and 23. However, only exometabolomic data from day 19 and 23 were used to quantitatively constrain the models. This is consistent with the established differentiation protocol used, where a 30-45% increase in cell number is observed during the first five days and therefore a steady state assumption was not considered valid during the early period in cell culture.

Steady state assumption. The assumption of a metabolic steady state for the differentiated dopaminergic neuronal cell culture in the latter period in cell culture is based on two observations. Firstly, in contrast to earlier stages, the cell number does not alter significantly in the last five days in culture (<3-4% increase). Secondly, it is known that the rate of neuronal differentiation reaches toward a plateau toward the end of the period in culture[54].

Exchange reaction rate. In the model, the unit of flux is μmol/gDW/hr, while the unit of metabolite concentration change is μmol. In order to transform an extracellular metabolite concentration change into a lower bound on the corresponding exchange reaction flux, we assumed that

$$flux = metabolite\ concentration\ change\ /\ cell\ dry\ weight \times cell\ number \times time$$

based on an established approach, implemented in Metabotools[4], a software suite for integration of metabolomic data with constraint-based models, integrated into the COBRA Toolbox[26].

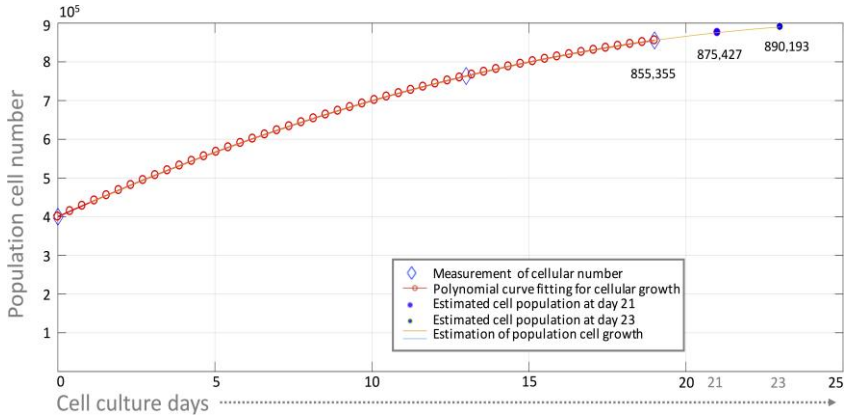

Figure S5: Measured and estimated cell numbers during neuronal differentiation
Cell culture numbers were measured at seeding (day 0) and day 13 and 19 of differentiation. The cell culture was seeded with a density of 400k cells per well. The cell number at day 21 and 23 was estimated by interpolation in order to enable normalisation of metabolic uptake and secretion rates.

Exchange reaction rate ranges. The measurements of metabolite concentration changes and the aforementioned cell culture parameters are associated with

measurement uncertainty. Therefore, this measurement uncertainty was propagated to uncertainty in the estimation of experimental exchange reaction rates. The exometabolomically derived exchange reaction ranges was therefore set to be between $v_{exp} - \sigma$, and $v_{exp} + \sigma$ where σ denotes the standard deviation in estimated experimental exchange reaction rates. For details on the exometabolomically derived exchange flux ranges for each measured metabolite, see Table S2.

S4 Model generation

A context-specific, flux-consistent, constraint-based metabolic model representative of the hNESC derived dopaminergic neuronal *in vitro* cell culture was generated using an overall approach based on established and novel Constraint-Based Reconstruction and Analysis methods[26].

S4.1 An overview of constraint-based modelling

All constraint-based modelling predictions are derived from optimisation problems, typically formulated in the form:

$$\begin{aligned} \min_{v \in \mathbb{R}^n} \quad & \psi(v) \\ \text{s.t.} \quad & Sv = 0 \\ & l \leq v \leq u, \end{aligned} \tag{2}$$

where $S \in \mathbb{R}^{m \times n}$ is a stoichiometric matrix of m metabolites and n reactions representing a biochemical 908 network, $v \in \mathbb{R}^n$ is the vector representing the flux through all of the reactions in a network and $\psi : \mathbb{R}^n \to \mathbb{R}$ is an objective function, which is typically convex. In a constraint-based metabolic model of reaction fluxes, the set of feasible steady-state flux vectors forms a polyhedral convex solution space, defined by the equality and inequality constraints in Equation (2), enabling optimisation of a variety of convex objective functions over this set.

The matrix S can be split horizontally into two matrices corresponding to internal, $N \in \mathbb{Z}^{m \times k}$, and external, $B \in \mathbb{R}^{m \times (n-k)}$, reactions, with corresponding internal and external rate vectors, $z \in \mathbb{R}^k$ and $w \in \mathbb{R}^{n-k}$. While all internal reactions are characterised by being mass and charge balanced, external reactions are, on the other hand, imbalanced reactions. External reactions are classified in sink, demand or exchange reactions. A demand reaction allows the accumulation of a compound. A sink reaction allows the production of a metabolite. Finally, A exchange reaction allows the

exchange of a metabolite across the extracellular boundary of a system, providing a mechanism to transfer metabolites between the environment and the extra-cellular fluid. Such reactions are distinct from transport reactions, which transfer metabolites between compartments within the model, including the extracellular compartment. Exchange reactions are added to a model to allow certain metabolites to be exchanged across the boundary of the system at variable rates.

The linear equality, $Sv = 0$ in Equation (2), represents mass balance for all the metabolites. This means, for each metabolite the rate of metabolite consumption is equal to the rate of metabolite production. In Equation (2), $Sv = 0$ implies that $Nz = -Bw$ where internal production plus external input equal internal consumption plus external output. For certain intracellular metabolites, those not exchanged across the boundary of the system, we assume they are at a steady-state, so we have $N_i z = 0$, where N_i denotes the i^{th} row of the internal stoichiometric matrix. Additional linear inequalities keep reaction rates between lower and upper bounds, l and u, respectively.

S4.2 The generic human metabolic model: Recon3.0 model

Given a generic reconstruction of human metabolism, not specific to any organ, tissue or cell type, a generic model of human metabolism was generated, using an established procedure[26].

Recon3D[7] is the latest and most comprehensive, manually-curated genome-scale reconstruction of human metabolism. Additionally, Recon3D provides information about gene-protein-reaction associations which associate each metabolic gene with the corresponding enzyme or enzyme complex and reaction in a Boolean manner. The largest stoichiometrically and flux consistent[26] part of Recon3D, termed Recon3.0model, was used as a generic model for generation of dopaminergic neuronal metabolic models. This generic model is divided into 9 cellular compartments and currently encompasses 2,248 open reading frames and 10,600 metabolic reactions involving 5,835 unique metabolites.

In each metabolic reaction, v_i, is constrained between a lower and an upper bound, $lb \leq v_i \leq ub$. The default reaction lower and upper bounds are commonly set based on

model characteristics and constraints value. Lower and upper bounds were set to include fluxes from metabolite concentration in the media, e.g., glucose flux rate based on media composition (-5,430.74 μmol/gDW/hr). Reactions can be reversible or irreversible. A reaction is said to be reversible in the case where it has a negative lb and a positive ub. When the lb is set to zero and the ub is a positive number the reaction proceeds in the forward direction. Similarly, when the ub is zero and the lb is a negative number the reaction occurs in the backward direction. The same works for exchange reactions: if a metabolite is taken up, the corresponding exchange reaction has zero as ub and a negative number as lb, whereas if it is secreted, the ub is a positive number and the lb is set to zero.

S4.3 Generation of the turnover model

Given the generic model, a turnover model was generated by applying constraints on the turnover rates of certain key cellular constituents of a dopaminergic neuron.

As described in supplementary information section S3.1, the minimum turnover requirement of a dopaminergic neuron was obtained from the literature and used to constrain the model as follows. When a biomass precursor was associated with a single degradation reaction, this reaction was set to irreversible in the direction of degradation, and 0.75 times the degradation rate d was set as the lower bound on that degradation reaction. A 25% relaxation of the lower bounds from the estimated degradation rate was used as standard to account for uncertainty in the data[66]. For the example of phosphatidylserine in supplementary information section S3.1, a lower bound was set on the phosphatidylserine decarboxylase reaction. When a biomass precursor could be metabolised through a reversible reaction, one direction of which corresponded to catabolism, this reaction was split into a pair of irreversible reactions and the turnover constraint applied to the catabolic direction.

When a biomass precursor could be degraded by more than one reaction, the sum total rates of degradation by all degradation reactions, was set to be greater than 0.75 times the degradation rate d, via an inequality of the form

$$v_1 + v_2 + \ldots + v_n \geq 0.75 \times d, \qquad (3)$$

with due consideration of reaction directionality. Support for inequalities, such as Equation 3, within constraint-based modelling problems, has been fully implemented

within the COBRA Toolbox[26]. In total, this approach resulted in 21 turnover constraints on single degradation reactions, and a further 8 turnover constraints, each on a set of degradation reactions, when the metabolite could be degraded by more than one pathway.

S4.4 Generation of the preconditioned model

Given the turnover model, a preconditioned model was generated by applying maximum metabolite uptake constraints and biochemically motivated constraints on certain otherwise reversible exchange reactions.

As described in supplementary information section S3.2, for each metabolite present in the fresh medium, the maximum metabolite uptake rate (μmol/gDW/hr) was calculated (Table S-3). This was then used to set the lower bound on the corresponding exchange reaction. The lower bounds on all other metabolite uptake reactions were set to zero, to reflect the assumption that no other metabolites, except those in the defined medium, were accessible to the *in vitro* culture. For each consumed metabolite, the upper bound on the corresponding exchange reaction is, by definition, set to zero.

Furthermore, some bounds on otherwise reversible exchange reactions were manually set to satisfy specific characteristics of a (neuronal) cell culture, e.g., the production of oxygen and glucose were disallowed by setting the upper bound on the corresponding exchange reaction to zero, so that only uptake became possible in the model. Also, the ionic transport reactions for sodium, calcium, potassium and iron, were closed ($l_j = u_j =: 0$). Of the components present in the fresh medium, 50 were used to qualitatively constraint the uptakes of the model. Furthermore, a set of reactions associated to dopaminergic neuronal metabolism were qualitatively constrained such as the production of neuromelanin, ATP, dopamine, GABA etc.

S4.5 Generation of the context-specific models

Given the preconditioned model, a context-specific model was generated by application of manually curated and omics derived constraints on the activity or inactivity of certain genes and reactions.

A core set of Recon3D genes and reactions were extracted by extensive manual curation of biochemical studies as being active or inactive in human dopaminergic neurons from the substantia nigra (supplementary information section S8). In addition to the specific data extracted from the literature, RNA-sequencing data from hNESC-derived dopaminergic neuronal *in vitro* cell culture, which is sensitive at genome-scale, was mapped into Recon3D to identify the genes that should be active in a dopaminergic neuronal reconstruction (supplementary information section S1.2).

A metabolic network formed from the set of core reactions alone is not necessarily flux consistent, that is, some reactions may not admit a non-zero steady-state flux. Therefore, we used the FASTCORE algorithm[71], implemented in the COBRA Toolbox[57] to generate a compact, flux-consistent model. This model returns a minimal number of extra reactions, beyond the core set, that are required to ensure the flux-consistency of the model. Therefore, the output is a context-specific, flux-consistent model.

S4.6 Generation of exometabolomically constrained models

Given the context-specific model, a set of exometabolomically constrained models were generated by selective application of constraints derived from quantitative measurements of fresh and spend cell culture medium. Exometabolomically derived exchange reaction ranges, for metabolites measured to be taken up from the fresh medium were used to generate an *uptake constrained model* (ModelUpt) to test its ability to predict the measured secreted metabolites. Exometabolomically derived exchange reaction ranges, for metabolites measured to be secreted into the medium were used to generate a *secretion constrained mode*l (ModelSec) to test its ability to predict uptaken metabolites. Furthermore, for each one of the measured metabolites, a *leave-one-out model* was generated, from the iNESC2DN, to test the ability to predict exchange of one metabolite measured, but left out of the set used to constrain the

model. The iNESC2DN model was generated from the context-specific model by including all constraints derived from the metabolomic data on uptaken and secreted metabolites. It is this iNESC2DN model that was subsequently used then to design future metabolomic experiments.

A given vector of exometabolomically derived exchange reaction rates $v_{exp} \in \mathbb{R}^n$, obtained as described in supplementary information section S3.3, may not be consistent with the feasible set of steady state fluxes defined in 2. Specifically, inconsistent with the set defined by the steady state constraint ($Sv = 0$) as well as the lower and upper bounds on each reaction $l \leq v \leq u$. Should this occur, we fitted the model to the experimental data, relaxing the constraints on the bounds of 2, that admits a steady state flux $v \in \mathbb{R}^n$, using the following quadratic optimisation problem

$$\begin{aligned} \min_{v,p,q \in \mathbb{R}^n} \quad & (v_{exp} - v)^T \mathrm{diag}(w_{exp})^{-1} (v_{exp} - v) + p^T \mathrm{diag}(w_l) p + q^T \mathrm{diag}(w_u) q \\ \text{s.t.} \quad & Sv = 0, \\ & l - p \leq v \leq u + q, \\ & 0 \leq p \\ & 0 \leq q \end{aligned} \tag{4}$$

where $p \in \mathbb{R}^n_{\geq 0}$ and $q \in \mathbb{R}^n_{\geq 0}$ are non-negative variables that permit relaxation of the lower and upper bound constraints, respectively. This formulation also allows for different weights to be input as parameters to Problem 4 to penalise deviation from experimentally measured mean fluxes, with $w_{exp} \in \mathbb{R}^n_{\geq 0}$, penalise relaxation of lower bounds, with $w_l \in \mathbb{R}^n_{\geq 0}$ and penalise relaxation of upper bounds, with $w_u \in \mathbb{R}^n_{\geq 0}$. For example, if the experimentally measured flux is actually the mean flux, then one could set w_{exp} to be the inverse of the variance on the experimental flux measurements, thereby increasing the penalty on deviation from an experimentally measured mean flux where the variance is lower. Certain lower or upper bounds might not be realistic to be relaxed, e.g., an essential amino acid can always be taken up but never secreted, therefore the upper bound on the corresponding exchange reaction must be zero.

S5 Model testing and characterisation

A selection of constraint-based modelling techniques were used to test the ability of *in silico* models to predict independent exometabolomic data. Let $\Omega := \{v \in \mathbb{R}^n \mid Sv = 0, l \leq v \leq u\}$ denote the set of steady-state flux vectors consistent with the constraints, and $\dim(\Omega)$ denote the number of linearly independent dimensions of this set. In Flux Balance Analysis (FBA) one obtains an optimal flux vector by choosing a coefficient

vector $c \in \mathbb{R}^n$, representing a biologically motivated linear objective $\psi(v) := c^T v$ (e.g. ATP production, dopamine secretion, etc.) and enforcing $v \in \Omega$. Since the correct coefficient vector is not known for neurons, we used alternative approaches to explore Ω. Flux Variability Analysis (FVA)[38], was used to find the *flux ranges* for each reaction rate by choosing a coefficient vector $c \in \mathbb{R}^n$ with one non-zero entry, then minimising and maximising $\psi(v) := c^T v$, for each reaction in turn. FVA was implemented in a computationally efficient manner using the fastFVA algorithm[21], within the COBRA Toolbox[26].

In addition, uniform sampling[72] was used to generate an unbiased characterisation of the set of steady-state flux vectors Ω. Uniform sampling provides a quantitative prediction of the probability of each quantitative flux value, between the same minimum and maximum flux predicted by flux variability analysis, assuming that each feasible steady-state flux vector is equiprobable. Unlike FBA and FVA, uniform sampling does not use an objective function when predicting steady-state fluxes. Uniform sampling was implemented using the Coordinate Hit-and-Run with Rounding (CHRR) algorithm[25], within the COBRA Toolbox[26], using the parameters $nSkip = \dim(\Omega)^2$ and $nSamples = 8 \times \dim(\Omega)$, which represent the number of samples skipped between stored samples, and the total number of stored samples obtained, respectively. FVA and uniform sampling were used to test whether various *in silico* models could predict the outcome of independent exometabolomic analyses (see Figure 5.2, and for all measured exchanged metabolites more comprehensively, see Figure S12 and S13).

Sparse Flux Balance Analysis approximately minimises the function $\psi(v) := \|v\|_0$ subject to $v \in \Omega$, and was used to predict the minimum number of reactions that are required to be active to satisfy the known metabolic demands on a dopaminergic neuron, as represented by the aforementioned dopaminergic neuron specific constraints on the steady-state flux space Ω. The SparseFBA algorithm is implemented in the COBRA Toolbox[26].

S6 Experiment design

S6.1 Exometabolomic experiment design

Using uniform sampling, we calculated the flux ranges of exchange reactions to predict a list of secreted metabolites to consider for targeted metabolomic analyses in future exometabolomic experiments. Furthermore, we prioritised this list of secreted metabolites by rank ordering it using two novel pipelines for optimal design of future exometabolomic experiments.

In the uncertainty reduction pipeline, illustrated in Figure 5.3a-c, our goal is to select the k rows of the covariance matrix that will explain as much uncertainty in the model as possible, as suggested by the uniform samples. More precisely, we seek to select a subset of k rows such that the k-dimensional volume spanned by these vectors is maximised. Computing this subset exactly is a difficult computational problem, and we instead use a heuristic, iterative method that greedily selects the row that has the maximum Euclidean distance to the subspace spanned by the rows selected already. For the first row, this reduces to selecting the row of the covariance matrix with largest Euclidean norm. The largest Euclidean norm of the covariance matrix of exchange reaction fluxes, was used to rank order the metabolic exchanges contributing the most uncertainty to iNESC2DN predictions (Figure 5.3d).

In the phenotypic perturbation pipeline, illustrated in Figure 5.3e-h, we predicted the exometabolomic changes most likely to occur following perturbation to internal reaction rates, as illustrated in (Figure 5.3h). Starting with the iNESC2DN model, the effects of two different perturbations were predicted: (i) deletion of the glucocerebrosidase (GBA1) gene, the gene most commonly associated with PD, and (ii) complete inhibition of mitochondrial complex I. For each reaction, a two-sample Kolmogorov-Smirnov test was used to check whether the sampled fluxes for perturbed and control models came from different distributions, with a 5% significance level. This test uses the maximum absolute difference between the cumulative distribution functions of the distributions of the two data vectors. For the j^{th} reaction, the test statistic is

$$D_j^* := \max_v j \left(|F\hat{c}\ (v_j) - F\hat{p}\ (v_j)|\right)$$

where $F\hat{_C}(v_j)$ is the proportion of control model sample flux values less than or equal to v_j and $F\hat{_P}(v_j)$ is the proportion of perturbed model sample flux values less than or equal to v_j.

S6.2 Conserved moieties and atom mapping

Where available, a molecular structure was obtained for each metabolite from the Virtual Metabolic Human database (www.vmh.life,[47]) and atom to atom mappings for each of the internal reaction of the iNESC2DN model were obtained using an atom mapping algorithm, the Reaction Decoder Tool[53], which performed optimally in a benchmarking exercise[52]. The atom mappings were then used to identify the metabolite structural moieties that are conserved despite all of the metabolic transformations in the iNESC2DN model. Moiety identification used an established algorithm[24], implemented within the COBRA Toolbox[26].

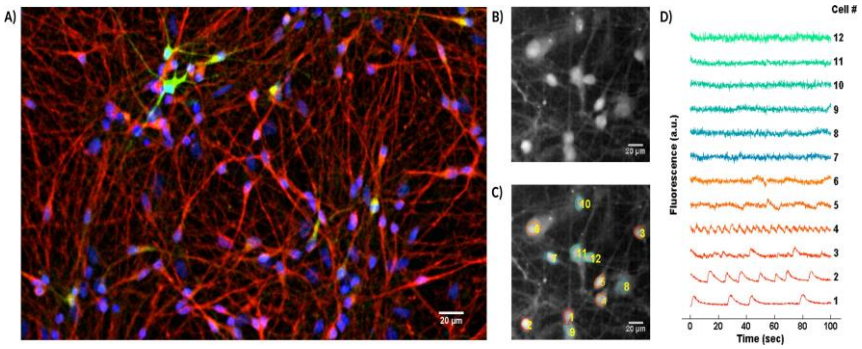

Figure S6: Immunostaining and calcium imaging.
Immunostaining of differentiated neurons and calcium imaging of spontaneously firing human neuroepithelial stem cell differentiated into dopaminergic neurons. (a) Immunostaining of a representative well at day 23, showing neurons positive for nuclei with Hoechst (blue), TUB□III (red) and TH (green); scale bar 20□m. (b) Mean frame of a field of view of representative neurons. (c) Automatic segmentation of neurons. (d) Fluorescence traces showing the spontaneous activity of individual segmented neurons.

Part II
Results
S7 Experimental results
S7.1 Cell culture

The differentiation of hNESCs into dopaminergic neurons was successfully accomplished. Differentiated neurons were identified by TUBβIII immunoreactivity. Neurons positive for tyrosine hydroxylase (TH) confirmed the presence of neurons capable of converting tyrosine to L-DOPA, the penultimate step in dopamine synthesis (Figure S6a). Analysis of calcium imaging data revealed spontaneously active neurons (Figure S6b, c, d).

S7.2 Transcriptomic data

Transcriptomic data contains a range of gene expression values. Some of the low expression values are certainly attributable to experimental noise or aborted transcripts, but for borderline expression values, it is a challenge to divide the corresponding genes into expressed or not expressed. Each gene with less than zero FPKM, on base-two logarithmic scale, was considered not expressed[59]. Each gene with FPKM higher than a threshold of zero, on base-two logarithmic scale, was considered expressed. Out of the 18,530 unique genes with expression levels reported in the transcriptomic data, 12,698 were considered to be expressed, based on the aforementioned threshold. However, only 1,202 were mapped into Recon3D (metabolic genes) and therefore included in the model. To test the viability of the selected transcriptomic data expressed in the *in vitro* culture and selected in Recon3D, a receiver operating characteristic (ROC) curve[23] was generated to qualitatively compare the expressed and not-expressed assignments from hNESC-derived dopaminergic neurons transcriptomic data against the active and inactive assignments for manually curated dopaminergic neuronal genes (supplementary information section S8 below), which we assume to be a true representation of dopaminergic neuronal gene expression (Figure S7). If a gene was considered to be active by manual curation and was also found to be expressed in transcriptomic data, it was considered a true positive (TP). The proportion of true positives that were correctly classified as positive, is given by the *true positive rate* (TPR)

$$TPR = TP / TP + FN'$$

where TN, FP and FN denote true negatives, false positives and false negatives, respectively. Likewise, the f*alse positive rate* (FPR) is

$$FPR = FP / FP + TN.$$

The true and false positive rates can vary depending on the threshold applied to distinguish between an expressed and a not-expressed gene. In the reconstruction, genes expressed above the threshold were assigned to be metabolically active and genes expressed below the threshold were not included as in the model, unless the corresponding reactions had to be included to generate a flux consistent model.

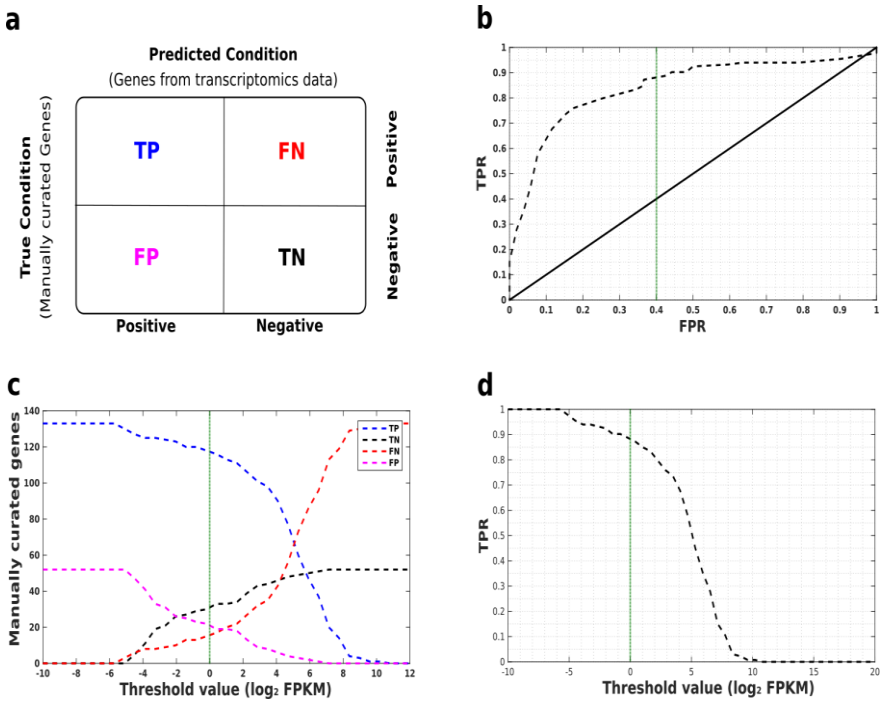

Figure S7: Manually curated genes compared with transcriptomic data.
(a) Confusion matrix illustrating the performance of the transcriptomic classification into active and inactive genes. TP - True Positive, TN - True Negative, FN - False Negative, FP - False Positive. (b) Receiver operating characteristic (ROC) curve. TPR - True Positive Rate, FPR - False Positive Rate.(c) Number of manually curated genes per threshold for each condition.(d) A true positive rate of 0.9 corresponded to a threshold

value of zero Fragments Per Kilobase of transcript per Million mapped reads (FPKM), on base-two logarithmic scale (green vertical line).

S7.3 Exometabolomic analysis

Medium characterisation. The manufacturers specification identifies a total of 57 different metabolites in the fresh culture medium, of which 24 were amines, 12 vitamins, 16 inorganic salts, 1 lipid, 2 nucleotides and 2 organic acids (Table S-4). Out of these 57 metabolites, 50 were present in the stoichiometrically and flux consistent generic model (Recon3Dmodel) and were omitted from further consideration. Of the omitted 7 metabolites, four inorganic salts (nitrate, vanadium, manganese and copper) were not present in the reconstruction (Recon3D), and a further three (magnesium, cyanocobalamin and selenite) did not correspond to any stoichiometrically and flux consistent reaction.

By running fresh medium samples in the organic acid (GC-MS) and amine (LC-MS) platforms, we were able to measure the absolute concentrations of both organic acids (glucose and pyruvic acid) and 22 of the 24 amines, known to be in the medium. This enabled us to test the concordance between the specifications of the medium manufacturer and the actual concentrations (Figure S8). Reduced glutathione and L-cystine are two amines that cannot be detected by the LC-MS platform. The remaining medium components are mainly inorganic salts and they were not measured.

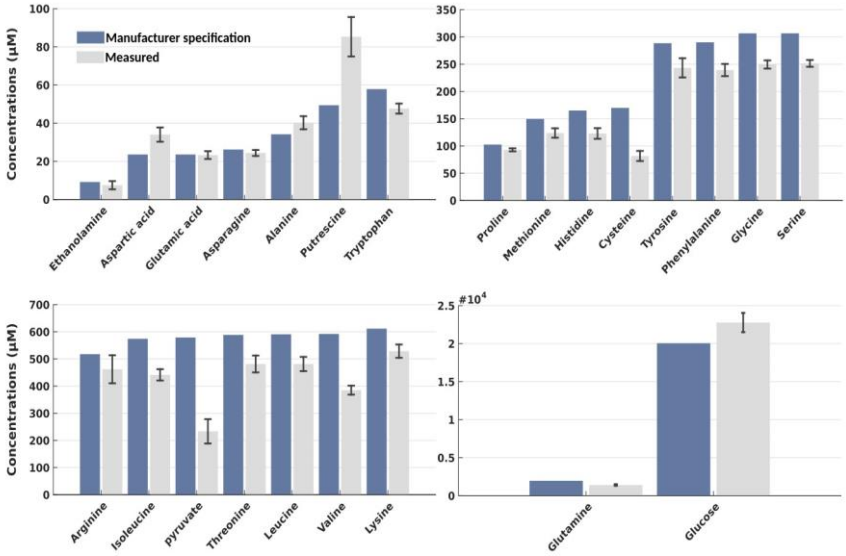

Figure S8: Validation of specified fresh medium concentrations.

Metabolite concentrations specified by the medium manufacturer (blue) compared to the absolute concentrations measured by mass spectrometry (grey). Some quantified metabolite concentrations, e.g., for cysteine, pyruvic acid, valine, aspartic acid and putrescine, significantly deviate from the manufacturers specifications.

S8 Reconstruction and manual curation

Active genes. Based on literature curation, a total of 252 metabolic genes were established to be active in dopaminergic neuronal metabolism (Table S-1). Out of these 252 genes, 20 are related to transport reactions, 6 to dopamine metabolism, 124 associated to mitochondria and 102 to central carbon metabolism. Significant effort was made to manually curate transport reactions as their presence or absence help to establish the idiosyncratic boundary conditions for any particular cell type. Out of the genes for transport reactions in Recon 2.04, biochemical literature on approximately half (118/255) were individually manually curated. From these 118 transporters, 20 were found to be present in the substantia nigra or substantia nigra pars compacta in human, mouse, or rat.

Active reactions. Based on literature curation, a total of 420 unique reactions were found to be active in dopaminergic neurons (Table S-2). However, 10 of these were excluded from the model generation process as they were either stoichiometrically or flux inconsistent. Included in these 420 reactions there are 69 from dopamine metabolism, 31 from an intersection the medium metabolites with the transport reactions associated with the 24 transport genes, 8 demand reactions for biomass precursors, 53 exchange reactions corresponding to medium metabolites, 5 exchange reactions from the metabolites being newly synthesised according to the exometabolomic data, and 160 reactions related to mitochondria and central carbon metabolism.

Inactive genes and reactions. Based on literature curation, a total of 148 genes were deemed to be inactive in neurons (Table S-1). These inactive genes were used to help determine the cutoff between expressed and non-expressed genes in the analysis of transcriptomic data (supplementary information section S1.2). Based on manual curation, a total of 211 metabolic reactions were considered to be inactive in the brain (Table S-2) and therefore were excluded from the model.

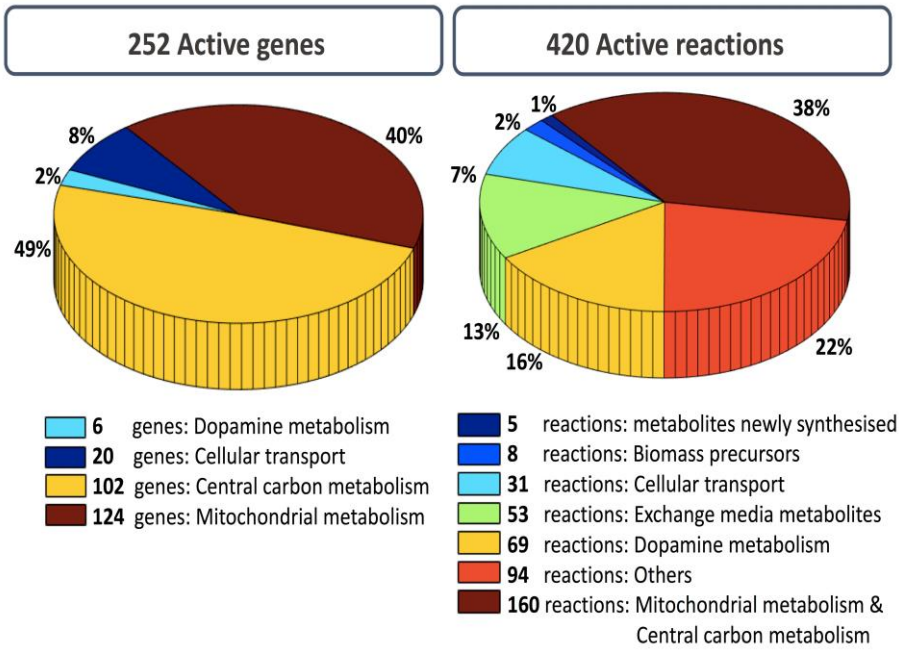

Figure S9: Classification of active reactions and genes by manual curation.
This manual curation result is partly a reflection of the availability of biochemical information on certain pathways, e.g., central metabolism, and partly a reflection of the pathways that were targeted for manual curation, e.g., dopamine metabolism.

Dopamine metabolism. Following manual curation of the literature[41, 58, 43, 44, 76, 14, 10, 69, 27, 45], 9 metabolites and 49 reactions were added to dopamine metabolism during the generation of Recon3D from Recon 2.04. These are 11 transport, 11 exchange, 19 metabolic and 8 demand reactions. In Recon3D, dopamine metabolism now includes 122 reactions in total (Figure S10). Out of these 122 reactions, we were able to collect evidence for the occurrence of 77 reactions in dopaminergic neurons that were also included in our reconstruction as active reactions: 42/49 newly added reactions and 35/73 dopamine-related reactions already present in Recon 2.04 (21 reactions from 'Tyrosine metabolism' subsystem, 1 reaction from 'Miscellaneous' subsystem, 4 reactions from 'Transport, extracellular' subsystem, 7 reactions from 'Exchange/demand reaction' subsystem, 1 reactions from 'Tetrahydrobiopterin metabolism' subsystem, 1 reaction from 'Phenylalanine metabolism' subsystem). For

many reactions (45/122) no clear information was found, therefore they were not included as active or inactive. Further information can be found in Table S-2.

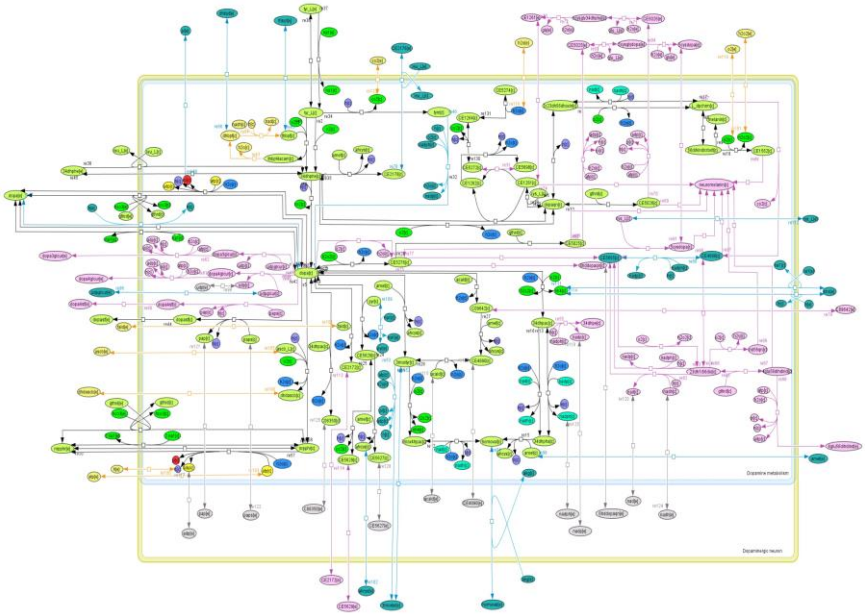

Figure S10: Reconstruction of dopamine metabolism.
Dopamine metabolism in Recon2.04 (green, blue) was refined and updated with newly added reactions (pink).

S9 Constraints

S9.1 Exometabolomic data

We performed a targeted metabolomic analysis and quantified metabolic differences with respect to time. Two platforms were selected, capable of detecting a total of 98 metabolites (74 metabolites from amines and amino acids platform and 24 from organic acid platform). Of the 50 metabolites, measured above the lower limit of detection, all were present in Recon3D. However one metabolite, glutaric acid (VMH), was not present in the stoichiometrically and flux consistent subset of Recon3D, designated Recon3.0model, and therefore, they were not further considered for computational modelling. From the remaining 49 metabolites, 24 were not previously present in the fresh medium 11.

S10 Generated models

The main characteristics of the different models generated along this process is given in Table S-5. A total of 6 main models were generated. Model generic correspond to Recon3.0model. The first four features define the composition of the metabolic network based on transcriptomic data and manual curation of reactions and genes. The last seven features define the range of fluxes through the network by differential application of constraints. A brief summary of each model is given below:

1. *Generic Recon3Dmodel*: A close approximation to the largest stoichiometrically and flux-consistent subset of Recon3D (5,835 metabolites and 10,600 reactions), named Recon3.0model in[7].

2. *Turnover* model: Recon3Dmodel with added constraints representing the cellular turnover. A total of twenty-one reactions were individually constrained. Furthermore, 26 reactions were associated with eight turnover constraints (Table S-2).

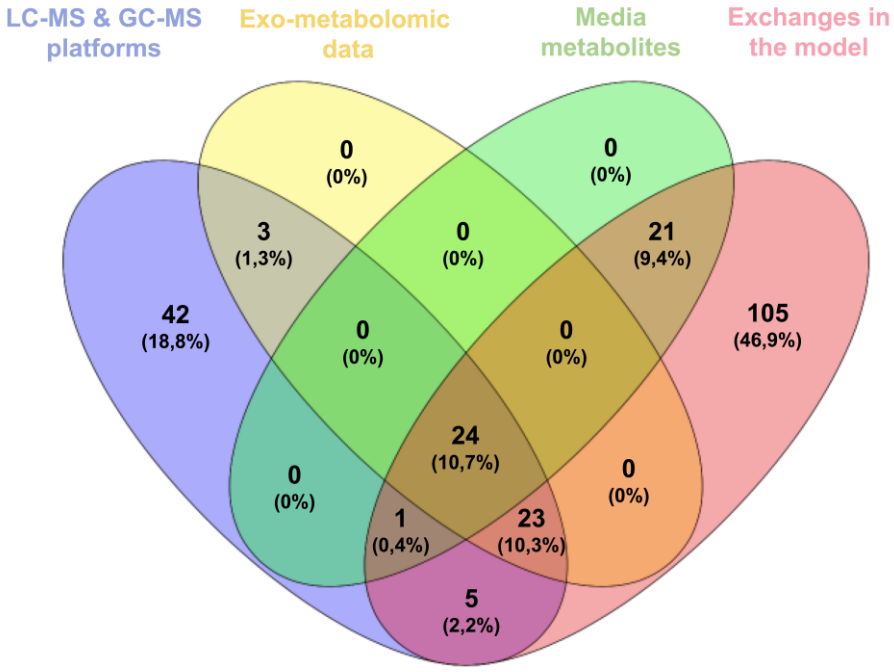

Figure S11: Venn diagram summarising metabolites.
A total of 98 metabolites were targeted by the selected LC-MS and GC-MS platforms (blue). Of these 98, only 50 were detected in the spent medium obtained to generate exometabolomic data (yellow). Of these 50 metabolites, 49 could be used to constrain the model as only one metabolite was not present in the stoichiometrically and flux consistent subset of Recon3D. Of these 49 metabolites, 25 were present in the fresh medium and 24 were synthesised by the cells and secreted into the spent medium. The final iNESC2DN model contains exchanges reactions for 179 metabolites (red), therefore there still remains 126 metabolites to target with exometabolomic platforms developed and applied in future.

3. *Preconditioned* model: Turnover model with added qualitative constraints for 46 fresh media metabolites. Exchange reactions corresponding to fresh media metabolites were open with a *lb* set less than zero, to the negative of the maximum concentration of each metabolite in the fresh media. Uptake reactions corresponding to metabolites not in the fresh media were closed (*lb* set to zero) (see Table S-3).

4. *Draft context-specific* model: Preconditioned model with added manual curation and integration of context-specific transcriptomic data, to generate a model consisting of 1776 metabolic reactions (see Tables S-2).

5. iNESC2DN model: Context-specific model with exometabolomic constraints added for 30 metabolites taken up and 19 metabolites secreted. This omits exometabolomic constraints on L-proline and L-serine, as the model would otherwise be infeasible.

6. ModelUpt: Context-specific model with added exometabolomic constraints for 30 metabolites measured to be taken up from the medium (see Table S-2).

7. ModelSec: Context-specific model with added exometabolomic constraints for 19 metabolites measured to be secreted into the medium (see Table S-2).

S11 Model testing

S11.1 Prediction of metabolite secretion rates

Figure 5.2a-c provides a comparison of measured and predicted metabolite secretion rates, for 3 representative metabolites, using ModelUpt, a context-specific model quantitatively constrained with exometabolomically derived constraints on secretion reaction rates. Figure S12 provides this comparison for all 29 metabolites measured to be secreted into the medium by the cell culture.

S11.2 Prediction of metabolite uptake rates

Figure 5.2d-f provides a comparison of measured and predicted metabolite uptake rates, for 3 representative metabolites, using ModelUpt, a context-specific model quantitatively constrained with exometabolomically derived constraints on uptake reaction rates. Figure S12 provides this comparison for all 19 metabolites measured to be uptaken from the fresh medium by the cell culture.

S12 Model characterisation

Figure S14 compares the number of reactions from each metabolic subsystem present in the Recon3.0 model, the iNESC2DN model and the minimal set of reactions required to be active to satisfy all of the iNESC2DN constraints. Figure 5.3b and 5.3h illustrate the reactions within the iNESC2DN model that are predicted to be perturbed as a result of GBA1 knockout and Complex I inhibition, respectively.

Part III
Discussion

S13 Characteristics of the iNESC2DN model

Tetrahydrobiopterin metabolism is an example of a metabololic subsystem critical for dopaminergic neuronal metabolism that is also represented in the iNESC2DN model. Tetrahydrobiopterin is absolutely required for the synthesis of monoamine neurotransmitters[28], including dopamine. The tetrahydrobiopterin biosynthetic pathway is thought to involve up to eight different proteins that support six alternate *de novo* and two alternate salvage pathways. The expression of these genes is highly correlated with each other and is particularly enriched within monoaminergic

neurons[28]. The first and limiting step in the tetrahydrobiopterin biosynthetic pathway is catalyzed by GTP cyclohydrolase I (GCH1). The expression of this gene is generally low and particularly heterogeneous across different populations of monoamine-containing neurons in humans and rodents, although GCH1 expression is a characteristic of nigrostriatal dopaminergic neurons[28]. The *in vitro* culture expresses GCH1 (log2(RPKM)>2) and therefore the corresponding Recon3D reaction gtp cyclohydrolase I (GTPCI) is also included in the iNESC2DN model. GTP cyclohydrolase I produces dihydroneopterin triphosphate (ahdt) and formic acid (for). In a subsequent reaction, 6-pyruvoyltetrahydropterin synthase (PTHPS) converts dihydroneopterin triphosphate (ahdt) into 6-pyruvoyltetrahydropterin (6pthp), which is a direct precursor of tetrahydrobiopterin (thbpt).

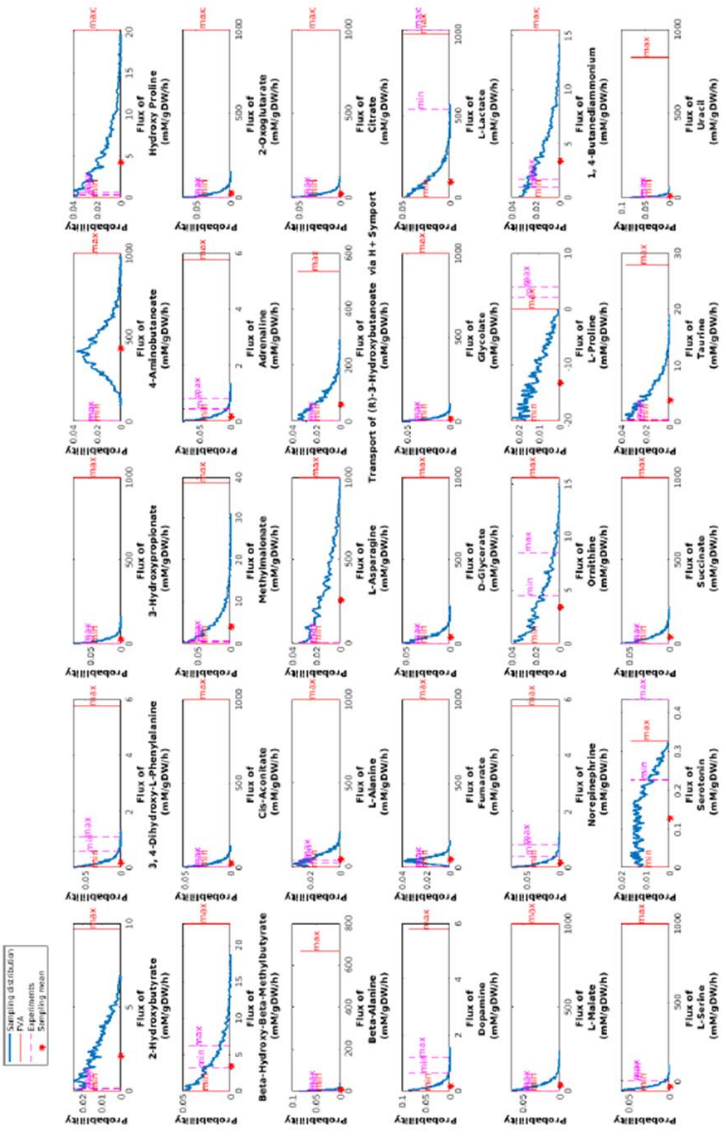

Figure S12: Comparison of predicted and measured metabolite secretion rates.
An uptake constrained model (ModelUpt) was tested for its ability to predict measured rates of 29 secreted metabolites, with three representatives illustrated in (a-c). A measured range for each exchange reaction rate (pink) was obtained from quantitative exometabolomic measurements and includes one standard deviation of measurement uncertainty. Predicted probability of exchange reaction flux obtained by uniform sampling (dark blue). Predicted exchange reaction flux, derived from the mean of the sampling distribution (red dot). Predicted maximum and minimum fluxes obtained by flux variability analysis (orange). The measured secretion reaction fluxes were within the range predicted by flux variability analysis of ModelUpt for 26 metabolites, and outside the range for 3 metabolites.

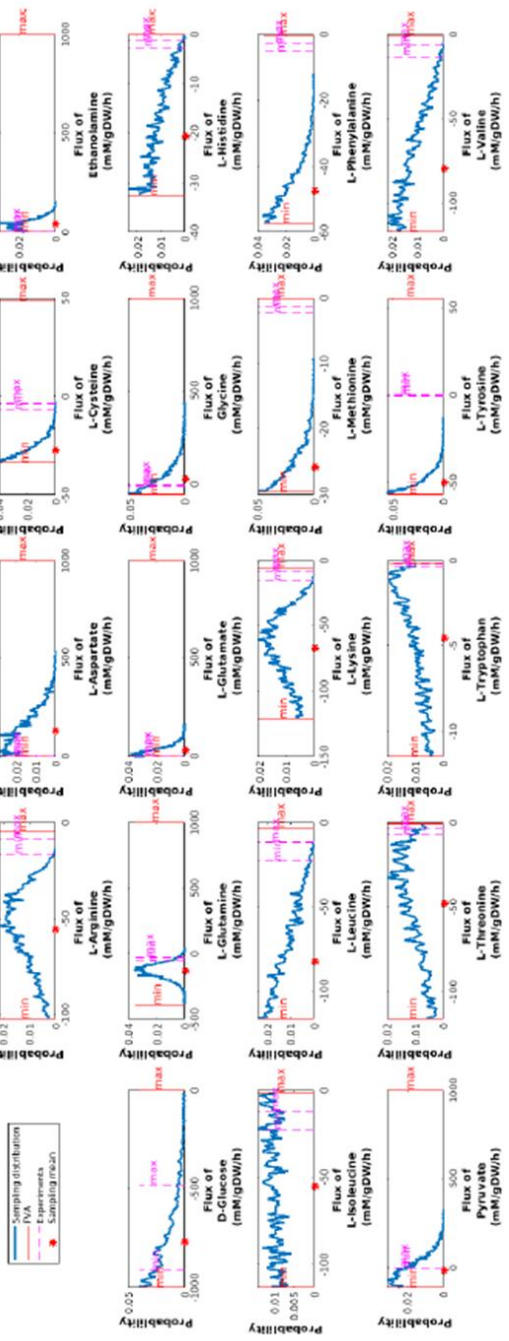

Figure S13: Comparison of predicted and measured metabolite uptake rates.
A secretion constrained model (ModelSec) to test its ability to predict measured rates of 19 metabolites measured to be taken up from the fresh medium. A measured range for each exchange reaction rate (pink) was obtained from quantitative exometabolomic measurements and includes one standard deviation of measurement uncertainty. Predicted probability of exchange reaction flux obtained by uniform sampling (dark blue). Predicted exchange reaction flux, derived from the mean of the sampling distribution (red dot). Predicted maximum and minimum fluxes obtained by flux variability analysis (orange). The measured uptake reaction fluxes were within the range predicted by flux variability analysis of ModelSec for 14 metabolites and outside the range for 5 metabolites.

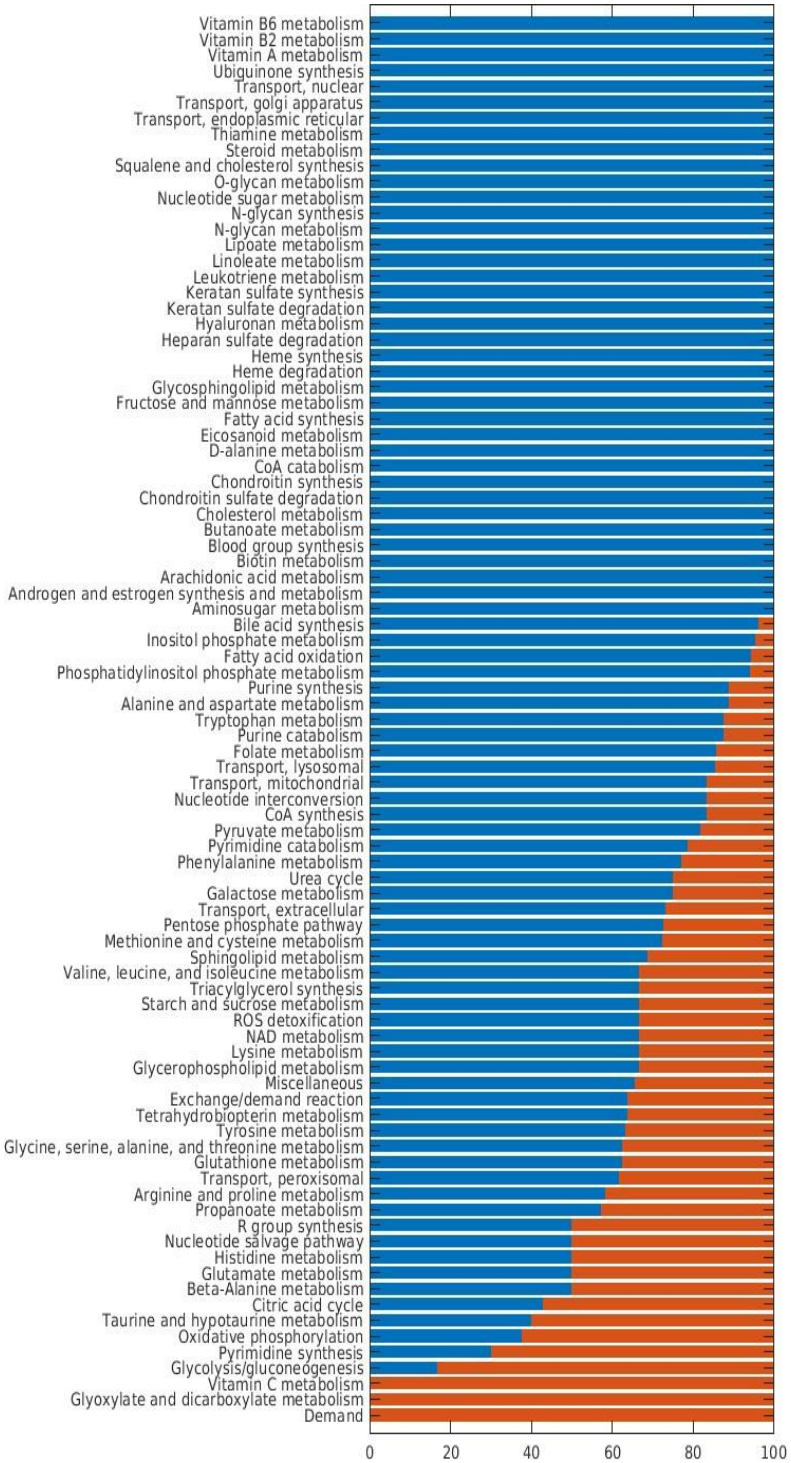
Vitamin B6 metabolism
Vitamin B2 metabolism
Vitamin A metabolism
Ubiquinone synthesis
Transport, nuclear
Transport, golgi apparatus
Transport, endoplasmic reticular
Thiamine metabolism
Steroid metabolism
Squalene and cholesterol synthesis
O-glycan metabolism
Nucleotide sugar metabolism
N-glycan synthesis
N-glycan metabolism
Lipoate metabolism
Linoleate metabolism
Leukotriene metabolism
Keratan sulfate synthesis
Keratan sulfate degradation
Hyaluronan metabolism
Heparan sulfate degradation
Heme synthesis
Heme degradation
Glycosphingolipid metabolism
Fructose and mannose metabolism
Fatty acid synthesis
Eicosanoid metabolism
D-alanine metabolism
CoA catabolism
Chondroitin synthesis
Chondroitin sulfate degradation
Cholesterol metabolism
Butanoate metabolism
Blood group synthesis
Biotin metabolism
Arachidonic acid metabolism
Androgen and estrogen synthesis and metabolism
Aminosugar metabolism
Bile acid synthesis
Inositol phosphate metabolism
Fatty acid oxidation
Phosphatidylinositol phosphate metabolism
Purine synthesis
Alanine and aspartate metabolism
Tryptophan metabolism
Purine catabolism
Folate metabolism
Transport, lysosomal
Transport, mitochondrial
Nucleotide interconversion
CoA synthesis
Pyruvate metabolism
Pyrimidine catabolism
Phenylalanine metabolism
Urea cycle
Galactose metabolism
Transport, extracellular
Pentose phosphate pathway
Methionine and cysteine metabolism
Sphingolipid metabolism
Valine, leucine, and isoleucine metabolism
Triacylglycerol synthesis
Starch and sucrose metabolism
ROS detoxification
NAD metabolism
Lysine metabolism
Glycerophospholipid metabolism
Miscellaneous
Exchange/demand reaction
Tetrahydrobiopterin metabolism
Tyrosine metabolism
Glycine, serine, alanine, and threonine metabolism
Glutathione metabolism
Transport, peroxisomal
Arginine and proline metabolism
Propanoate metabolism
R group synthesis
Nucleotide salvage pathway
Histidine metabolism
Glutamate metabolism
Beta-Alanine metabolism
Citric acid cycle
Taurine and hypotaurine metabolism
Oxidative phosphorylation
Pyrimidine synthesis
Glycolysis/gluconeogenesis
Vitamin C metabolism
Glyoxylate and dicarboxylate metabolism
Demand
0
20
40
60
80
100

Figure S14: Minimal flux metabolic subsystems of the iNESC2DN model.
Comparison of the fraction of reactions in (red) and out (blue) of the minimal flux vector in each metabolic subsystem of the iNESC2DN model.

S14 Metabolic assays

The quality of the experimental measurements was assessed by comparing the measured and supplier reported concentration values (Fig. S8). Based on this comparison, for most of the measured metabolites, the measurements were obtained within a similar concentration value (20%) reported in fresh culture media. However, some measurements (e.g. cysteine, pyruvic acid, valine, aspartic acid and putrescine) demonstrated larger differences between measured and supplier's concentrations. There can be several explanations for the discrepancy between specified and measured quantities. Some compounds may undergo easily reactions with other elements/compounds in their environment due to their reductive and/or oxidative nature. For instance, the thiol group of the cysteine is reactive both with oxidants and reductants as well as it has high affinity for metals[51]. Therefore, it can be very difficult to determine the quantity of free cysteine residues after protein hydrolysis unless the thiol group of the molecule is not stabilised by extensive chemical derivatisation procedures[1]. This could easily explain the observation of a lower value for the measured concentration in comparison to the reported value 8. Under oxidative and low pH conditions of the incubator, free cysteine may have been converted into different compounds which were not targeted during our analysis. The discrepancy can be due to the incomplete knowledge on the composition and concentration of medium supplements. B21 medium supplement contains a confidential amount of putrescine which may have contributed to the large increase in the measured concentrations.

It has been previously shown that the concentration of pyruvic acid can be reduced in blood by its reaction with bisulphite-binding substances. This can be also true for the pyruvic acid in fresh culture medium where there are several substances with the bisulphite-binding characteristics. In general, it is challenging to determine an overall reference point for the absolute concentrations as many factors may contribute to the in accuracy of the measurements. One of these factors is the difference in measurement uncertainties between different analytical methods. Previously, the measurement accuracy of ELISA against a validated tandem LC-MS

method has been evaluated and several differences were observed. The analytical assays that were used to report the concentration values in the medium samples by the suppliers may exhibit a difference in uncertainty in comparison to our analytical platforms. At this point, there is still a lack of certain standardisation for absolute concentration measurements among different analytical laboratories which have to be compiled under Good Laboratory Practice.

The absolute quantification of fluxes is advantageous for the training and validation of a metabolic model. However, the high chemical diversity and broad concentration range of the endogenous metabolites complicates the simultaneous quantification of many metabolites with one analytical methodology[56]. Due to its high selectivity and large dynamic range, mass spectrometry in combination with conventional separation techniques such liquid chromatography (LC), gas chromatography (GC) or capillary electrophoresis (CE) are the most popular methodologies in quantitative metabolomics.

S15 Analytical chemistry considerations

It is not possible for one analytical platform to quantify the concentration of all of the metabolites predicted to be secreted by the iNESC2DN model, because of the differences in their solubility, mass, endogenous concentration levels and volatility[22]. For selective and sensitive detection of diverse chemical classes of metabolites, several mass spectrometry (MS) based analytical platforms have been developed and reviewed extensively[6]. For the coverage of a broad group of hydrophilic metabolites such as amines and amino acids, carboxylic acids, sugars, nucleobases/nucleosides/nucleotides several hydrophilic interaction chromatography coupled mass spectrometry (HILIC-MS) platforms have been published and applied in cell culture and body fluids[50, 19, 75, 77, 70]. For the analysis of specific hydrophilic classes, it has been also a possibility to combine several chemical derivatisation techniques based on the functional group of the metabolites and achieve more retention and sensitivity on traditional reverse-phase liquid chromatography coupled mass spectrometry (RPLC-MS) [60, 73, 20].

For the separation of sugars and volatile metabolites gas chromatography coupled mass spectrometry (GC-MS) is a complementary method with its separation

efficiency for the stereoisomers of pentose and hexose sugar[32, 29, 68]. Nevertheless, GC-MS analysis requires chemical derivatisation for sugars which is suited for reducing the amount of several conformational isomers as well as increasing their volatility. For lipophilic metabolites, as similar to hydrophilic metabolites, there are analytical methods with broad coverage of different lipid classes[55, 74, 8, 11, 63, 9]. However, for certain lipid classes, such as oxylipins and isoprostanes[61, 16, 2], sphingolipid[42], bile acids[17, 34], cholesterol and cholesterol esters[37] and prenol lipids[18] more targeted RPLC-MS methods have been developed and validated in the literature.

To be able to generate the absolute concentration values of the metabolites, an efficient calibration strategy should be included with the authentic chemical and stable isotope labelled internal standards for each target metabolite or the target chemical class[62]. For this purpose the predictions of the *in silico* model will be an important asset to define the key target metabolites in the metabolic network for the calibration samples and thereby helping the right choice of the analytical platforms for the design of metabolomic experiments.

Supplementary tables.

Table S1. Literature curation showing evidence of activity, or inactivity of 252 genes.

EntrezGeneID (Active)	EntrezGeneID (Inactive)
38	586
39	1717
43	3156
226	6566
240	9194
241	10449
292	5409
384	128
412	222
498	1109
622	1544
840	1551
1152	1553
1160	1555
1583	1557
1588	1559
1593	1562
1607	1572
1630	1576
1737	1577
1738	1582
1743	1585
1757	1586
2023	1621
2026	2180
2052	2571
2074	2572
2108	2632
2109	2670
2110	2819
2222	2880
2246	3028
2261	3158
2271	3283

EntrezGeneID (Active)	EntrezGeneID (Inactive)
2539	3284
2597	3292
2629	3293
2645	3294
2646	3295
2720	3764
2739	5091
2747	5161
2820	5409
2821	5834
2932	6241
3098	6296
3099	6518
3101	6519
3170	6530
3479	6542
3763	6580
3939	7299
3945	7350
4047	7923
4190	8529
4191	8630
4929	9154
4967	10005
5053	10165
5106	10202
5160	10249
5162	10965
5209	10998
5211	11001
5214	11283
5223	23597
5226	26002
5315	26027
5337	26227
5527	28965
6342	51144
6515	51170
6821	51171

EntrezGeneID (Active)	EntrezGeneID (Inactive)
6853	51478
6888	51703
7084	54988
8050	55856
8802	55902
8803	57016
8878	57030
10059	64078
10135	64816
10797	64902
10858	66002
11332	79611
22934	80221
23761	81616
25796	83884
51552	84532
54550	93034
55669	93517
57084	114570
57194	116280
57704	117140
64080	121210
64802	122970
80210	123880
115827	126410
126328	134530
130752	197320
548596	246210
100133941	257200
18	267020
217	284490
219	340810
223	341390
224	345280
501	348160
539	376500
847	641370
1327	277
1329	278

EntrezGeneID (Active)	EntrezGeneID (Inactive)
1337	7364
1339	7365
1340	9426
1345	10720
1346	54575
1347	54577
1349	54579
1350	54657
1351	64711
1384	91227
1431	94033
1468	114770
1537	116080
2744	116180
2746	124980
2805	125210
2806	133690
2876	153200
2879	155180
2936	158840
3417	203610
3418	253180
3419	266740
3420	338600
3421	339220
4199	348930
4200	360200
4512	389020
4513	441280
4514	646490
4519	653600
4535	728440
4536	100140000
4537	100530000
4538	100530000
4539	102720000
4540	
4541	
4694	

EntrezGeneID (Active)	EntrezGeneID (Inactive)
4695	
4696	
4697	
4698	
4700	
4701	
4702	
4704	
4705	
4706	
4707	
4708	
4709	
4710	
4711	
4712	
4713	
4714	
4715	
4716	
4717	
4718	
4719	
4720	
4722	
4723	
4724	
4725	
4726	
4728	
4729	
4731	
4942	
6389	
6390	
6391	
6392	
6648	
7351	

EntrezGeneID (Active)	EntrezGeneID (Inactive)
7381	
7384	
7385	
7386	
7388	
7991	
8402	
8604	
8659	
9016	
9167	
9377	
9481	
10400	
10476	
10873	
10935	
10975	
23530	
27089	
27165	
29796	
51079	
54539	
55967	
56267	
79751	
80025	
83733	
84701	
125965	
126328	
170712	
341947	
349565	
374291	
1644	
4128	
4129	

EntrezGeneID (Active)	EntrezGeneID (Inactive)
6818	
7054	
9588	
19	
366	
3767	
4891	
5947	
6505	
6529	
6535	
6538	
6546	
6581	
6582	
6833	
10060	
81539	
84889	
206358	
6511	
6531	
6571	

Table S2. Metabolic reactions (445) in dopaminergic neurons.

Reaction abbreviation	Reaction description	Reaction formula
EX_phe_L[e]	exchange reaction for L-phenylalanine	phe_L[e]<=>
EX_tyr_L[e]	L-Tyrosine exchange	tyr_L[e]<=>
EX_dopa[e]	Dopamine exchange	dopa[e]<=>
EX_34dhphe[e]	3,4-Dihydroxy-L-phenylalanine exchange	34dhphe[e]<=> 34dhphe[c]
EX_glu_L[e]	Predicted informative metabolites	glu_L[e]<=>
EX_dopasf[e]	Dopamine 3-O-sulfate exchange	dopasf[e]<=>
EX_dopa4sf[e]	Dopamine 4-O-sulfate exchange	dopa4sf[e]<=>
EX_dopa4glcur[e]	Dopamine 4-O-glucuronide exchange	dopa4glcur[e]<=>
EX_dopa3glcur[e]	Dopamine 3-O-glucuronide exchange	dopa3glcur[e]<=>
r0399	L-Phenylalanine,tetrahydrobiopterin:oxygen oxidoreductase [4-hydroxylating]	o2[c]+ thbpt[c]+ phe_L[c]-> tyr_L[c]+ thbpt4acam[c]
TYR3MO2	tyrosine 3-monooxygenase	o2[c]+ thbpt[c]+ tyr_L[c]-> 34dhphe[c]+ thbpt4acam[c]
DHPR	6,7-dihydropteridine reductase	h[c]+ nadh[c]+ dhbpt[c]-> nad[c]+ thbpt[c]
3HLYTCL	3-Hydroxy-L-tyrosine carboxy-lyase	h[c]+ 34dhphe[c]-> co2[c]+ dopa[c]
DOPAt4_2_r	Dopamine reversible transport in via sodium symport [1:2]	2.0 na1[e]+ dopa[e]<=> 2.0 na1[c]+ dopa[c]
DOPASFt	Dopamine 3-0-sulfate transport [diffusion]	dopasf[c]-> dopasf[e]
DOPA4SFt	Dopamine 4-0-sulfate transport [diffusion]	dopa4sf[c]-> dopa4sf[e]
DOPA4GLCURt	Dopamine 4-O-glucuronide transport	dopa4glcur[c]+h2o[c]+ atp[c]-> dopa4glcur[e]+ adp[c]+ pi[c]+ h[c]
DOPA3GLCURt	Dopamine 3-O-glucuronide transport	dopa3glcur[c]+ h2o[c]+ atp[c]-> dopa3glcur[e]+ adp[c]+ pi[c]+ h[c]
TYRCBOX	L-Tyrosine carboxy-lyase	h[c]+ tyr_L[c]-> co2[c]+ tym[c]
DOPAc	formation of dopamine	o2[c]+ h[c]+ nadph[c]+ tym[c]-> h2o[c]+ nadp[c]+ dopa[c]
DOPAVESSEC	Dopamine secretion via secretory vesicle [ATP driven]	h2o[c]+ atp[c]+ dopa[c]-> h[c]+ adp[c]+ pi[c]+ dopa[e]
42A12BOOX	4-[2-Aminoethyl]-1,2-benzenediol:oxygen oxidoreductase[deaminating][flavin-containing]	h2o[c]+ o2[c]+ dopa[c]-> h2o2[c]+ nh4[c]+ 34dhpac[c]
34DHPEAR	3,4-Dihydroxyphenylethanol:NADP+ reductase	34dhpac[c]+ nadph[c]+ h[c]-> 34dhpe[c]+ nadp[c]
34DHPLACOX	3,4-Dihydroxyphenylacetaldehyde:NAD+ oxidoreductase	h2o[c]+ nad[c]+ 34dhpac[c]-> 2.0 h[c]+ nadh[c]+ 34dhpha[c]
34DHPLACOX_NADP_	3,4-Dihydroxyphenylacetaldehyde:NADP+ oxidoreductase	h2o[c]+ nadp[c]+ 34dhpac[c]<=> 2.0 h[c]+ nadph[c]+ 34dhpha[c]
EX_34dhpha[e]	exchange for 34dhpha	34dhpha[e]<=>
DOPASULT	Dopamine Sulfotransferase	paps[c]+ dopa[c]-> h[c]+ pap[c]+ dopasf[c]
DOPASULT4	Dopamine 4-O-Sulfotransferase	paps[c]+ dopa[c]-> h[c]+ pap[c]+ dopa4sf[c]
UDPG4DOPA	Dopamine 4-O-Glucuronidation	udpglcur[c]+ dopa[c]-> udp[c]+ dopa4glcur[c]
UDPG3DOPA	Dopamine 3-O-Glucuronidation	udpglcur[c]+ dopa[c]-> udp[c]+ dopa3glcur[c]
RE3201C	RE3201	o2[c]+ 56dihindlcrbxlt[c]-> h2o2[c]+ CE1562[c]
DCT	Dopachrome tautomerase	L_dpchrm[c]<=> 56dihindlcrbxlt[c]
DOPACHRMISO	L-dopachrome isomerase 1	o2[c]+ 2.0 2c23dh56dhoxin[c]-> 2.0 h2o[c]+ 2.0 L_dpchrm[c]
RE3198C	RE3198	h[c]+ nadh[c]+ L_dpchrm[c]<=> nad[c]+ 2c23dh56dhoxin[c]
DOPACHRMDC	L-dopachrome decarboxylation	L_dpchrm[c]-> co2[c]+ CE4888[c]
DOPAQNISO1	Dopaquinone isomerase 1	dopaqn[c]<=> h[c]+ 2c23dh56dhoxin[c]

Reaction abbreviation	Reaction description	Reaction formula
RE1917C	RE1917	dopaqn[c] + CE1261[c] <=> 34dhphe[c] + CE1262[c]
TYRDHINDOX	Tyrosinase: 5,6-dihydroxyindole oxygen oxidoreductase	2.0 CE4888[c]+ o2[c]-> 2.0 h2o[c]+ 2.0 ind56qn[c]
DACT	2,3-dihydro-1H-indole-5,6-dione tautomerization	23dh1i56dio[c]<=> CE4888[c]
NADPQNOXR	DT-diaphorase: NADP quinone oxireductase	nadph[c]+ h[c]+ 23dh1i56dio[c]-> nadp[c]+ CE5665[c]
NADQNOXR	DT-diaphorase: NAD quinone oxireductase	nadh[c]+ h[c]+ 23dh1i56dio[c]-> nad[c]+ CE5665[c]
LACROX	leukoaminochrome autoxidation	CE5665[c]+ o2[c]-> 23dh1i56dio[c]+ h2o2[c]
RE2526C	RE2526	h[c]+ nadph[c]+ CE4888[c]<=> nadp[c]+ CE5665[c]
RE2296C	RE2296	gthrd[c]+ CE5276[c]<=> CE5025[c]
CE5025t	transport of 5-S-glutathionyl-dopamine	CE5025[c]+ atp[c]+ h2o[c]-> CE5025 [e]+ adp[c]+ pi[c]+ h[c]
EX_CE5025[e]	5-S-glutathionyl-dopamine exchange	CE5025[e]<=>
DOPAOQCYS	Dopamine-o-quinone cysteine addition	cys_L[c]+ CE5276[c]<=> 5cysdopa[c]
5CYSDOPAt	transport of 5-S-cysteinyldopamine	5cysdopa[c]<=> 5cysdopa [e]
EX_5cysdopa[e]	5-S-cysteinyldopamine exchange	5cysdopa[e]<=>
RE1916C	RE1916	gthrd[c]+ dopaqn[c]<=> CE5026[c]
CE5026t	transport of 5-S-glutathionyl-L-DOPA	CE5026[c]+ h2o[c]+ atp[c]<=> CE5026[e]+ adp[c]+ pi[c]+ h[c]
EX_CE5026[e]	5-S-glutathionyl-L-DOPA exchange	CE5026[e]->
CE1261t	transport of 5-S-cysteinyldopa	CE1261[c]<=> CE1261 [e]
EX_CE1261[e]	CE1261 exchange	CE1261[e]<=>
4GLU56DIHDINDt	transport of 4-s-glutathionyl-5,6-dihydroxyindoline	4glu56dihdind[c]+ h2o[c]+ atp[c]<=> 4glu56dihdind[e]+ adp[c]+ pi[c]+ h[c]
EX_4glu56dihdind[e]	4-s-glutathionyl-5,6-dihydroxyindoline exchange	4glu56dihdind[e]<=>
DOPAtu	Dopamine uniport	dopa[e]<=> dopa[c]
RE1918C	RE1918	dopa[c]+ acald[c]<=> h2o[c]+ C09642[c]
C09642te	salsolinol transport uniport	C09642[c]<=> C09642[e]
EX_C09642[e]	C09642[e]exchange	C09642[e]<=>
CE5629t	transport of 6,7-dihydroxy-1,2,3,4-tetrahydroisoquinoline	CE5629[c]<=> CE5629[e]
EX_CE5629[e]	exchange for 6,7-dihydroxy-1,2,3,4-tetrahydroisoquinoline	CE5629[e]<=>
RE1921C	RE1921	CE5626[c]<=> 2.0 h[c]+ co2[c]+ CE5629[c]
RE1919C	RE1919	pyr[c]+ dopa[c]<=> h2o[c]+ CE5626[c]
RE3095C	RE3095	h2o2[c]+ dopa[c]<=> 2.0 h2o[c]+ CE5276[c]
RE2130C	RE2130	dopa[c]+ fald[c]<=> h2o[c]+ CE2172[c]
CE2172t	transport of 6,7-dihydroxy-1,2,3,4-tetrahydroisoquinoline	CE2172[c]<=> CE2172[e]
EX_CE2172[e]	exchange for 6,7-dihydroxy-1,2,3,4-tetrahydroisoquinoline	CE2172[e]<=>
DOPACCL	dopamine o-quinone cyclization	CE5276[c]-> CE5665[c]
DM_CE1261[c]	neuromelanin production from 5-S-cysteinyldopa	
DM_4glu56dihdind[c]	neuromelanin production from 4-s-glutathionyl-5,6-dihydroxyindoline	
DM_5cysdopa[c]	neuromelanin production from 5-S-cysteinyldopamine	
DM_CE1562[c]	neuromelanin production from 5,6-indolequinone-2-carboxylate	
DM_CE4888[c]	neuromelanin production from CE4888	

Reaction abbreviation	Reaction description	Reaction formula
DM_CE5025[c]	neuromelanin production from 5-S-glutathionyl-dopamine	
DM_CE5026[c]	neuromelanin production from 5-S-glutathionyl-L-DOPA	
DM_ind56qn[c]		
ALAt4		na1[e]+ ala_L[e] -> na1[c]+ ala_L[c]
ARGtD		arg_L[e] <=> arg_L[c]
ASCBSVCTtc		h2o[c]+ atp[c]+ 2 na1[e]+ ascb_L[e] -> adp[c]+ h[c]+ pi[c]+ 2 na1[c]+ ascb_L[c]
ASCBt4		na1[e]+ ascb_L[e] <=> na1[c]+ ascb_L[c]
ASNt4		na1[e]+ asn_L[e] -> na1[c]+ asn_L[c]
ASPDt6		h[e]+ 3 na1[e]+ asp_D[e]+ k[c] -> h[c]+ 3 na1[c]+ asp_D[c]+ k[e]
ASPt6		h[e]+ 3 na1[e]+ k[c]+ asp_L[e] -> h[c]+ 3 na1[c]+ asp_L[c]+ k[e]
CAt7r		3 na1[e]+ ca2[c] <=> 3 na1[c]+ ca2[e]
CHOLtu		chol[e] <=> chol[c]
CREATt4_2_r		2 na1[e]+ creat[e] <=> 2 na1[c]+ creat[c]
GLNt4		na1[e]+ gln_L[e] -> na1[c]+ gln_L[c]
GLUt6		h[e]+ 3 na1[e]+ k[c]+ glu_L[e] -> h[c]+ 3 na1[c]+ glu_L[c]+ k[e]
GLYt2r		h[e]+ gly[e] <=> h[c]+ gly[c]
GLYt4		na1[e]+ gly[e] -> na1[c]+ gly[c]
HMR_9613		2 na1[e]+ 4abut[e]+ cl[e] -> 2 na1[c]+ 4abut[c]+ cl[c]
HMR_9614		na1[e]+ dopa[e] -> na1[c]+ dopa[c]
HOMt4		na1[e]+ hom_L[e] -> na1[c]+ hom_L[c]
KCC2t		nh4[e]+ cl[e] <=> nh4[c]+ cl[c]
KCCt		k[e]+ cl[e] <=> k[c]+ cl[c]
LEUt4		na1[e]+ leu_L[e] -> na1[c]+ leu_L[c]
LYStiDF		lys_L[e] -> lys_L[c]
METt4		na1[e]+ met_L[e] -> na1[c]+ met_L[c]
PHEt4		na1[e]+ phe_L[e] -> na1[c]+ phe_L[c]
PROt2r		h[e]+ pro_L[e] <=> h[c]+ pro_L[c]
PROt4		na1[e]+ pro_L[e] -> na1[c]+ pro_L[c]
SELMETHte		na1[e]+ selmeth[e] -> na1[c]+ selmeth[c]
SERt4		na1[e]+ ser_L[e] -> na1[c]+ ser_L[c]
THRt4		na1[e]+ thr_L[e] -> na1[c]+ thr_L[c]
r1492		k[c] -> k[e]
r1518		h2o[c]+ atp[c]+ lnlc[c] -> adp[c]+ h[c]+ pi[c]+ lnlc[e]
r2471		h[e]+ ser_L[e] -> h[c]+ ser_L[c]
DM_pe_hs[c]		
EX_btn[e]		
EX_ascb_L[e]		
EX_chol[e]		
EX_fol[e]		

Reaction abbreviation	Reaction description	Reaction formula
EX_glc_D[e]		
EX_gly[e]		
EX_gthrd[e]		
EX_glu_L[e]		
EX_etha[e]		
EX_hxan[e]		
EX_tyr_L[e]		
EX_phe_L[e]		
EX_ala_L[e]		
EX_pro_L[e]		
EX_thr_L[e]		
EX_asn_L[e]		
EX_ile_L[e]		
EX_his_L[e]		
EX_lys_L[e]		
EX_ser_L[e]		
EX_asp_L[e]		
EX_Lcystin[e]		
EX_pnto_R[e]		
EX_inost[e]		
EX_thm[e]		
EX_pydxn[e]		
EX_pyr[e]		
EX_ribflv[e]		
EX_thymd[e]		
EX_ca2[e]		
EX_cl[e]		
EX_arg_L[e]		
EX_M02482[e]		
EX_cys_L[e]		
EX_k[e]		
EX_na1[e]		
EX_hco3[e]		
EX_gln_L[e]		
EX_lnlc[e]		
EX_leu_L[e]		
EX_met_L[e]		
EX_val_L[e]		
EX_trp_L[e]		

Reaction abbreviation	Reaction description	Reaction formula
EX_HC02172[e]		
EX_ncam[e]		
EX_ptrc[e]		
EX_pi[e]		
EX_so4[e]		
EX_lipoate[e]		
EX_M02887[e]		
EX_fe3[e]		
EX_nh4[e]		
EX_gal[e]		
EX_orn[e]		
EX_lac_L[e]		
EX_cit[e]		
EX_CE2028[e]		
EX_succ[e]		
EX_o2[e]	exchange reaction for oxygen	o2[e]<=>
H2Ot	H2O transport via diffusion	h2o[e]<=> h2o[c]
O2t	o2 transport [diffusion]	o2[e]<=> o2[c]
CO2t	CO2 transporter via diffusion	co2[e]<=> co2[c]
EX_co2[e]	CO2 exchange	co2[e]<=>
EX_h2o[e]	H2O exchange	h2o[e]<=>
GBAl	glucocerebrosidase	h2o[l]+ gluside_hs[l] -> crm_hs[l]+ glc_D[l]
GTPCI	GTP cyclohydrolase I	h2o[c]+ gtp[c]-> h[c]+ for[c]+ ahdt[c]
PTHPS	6-pyruvoyltetrahydropterin synthase	ahdt[c]-> pppi[c]+ 6pthp[c]
SPR	sepiapterin reductase	2.0 h[c]+ 2.0 nadph[c]+ 6pthp[c]-> 2.0 nadp[c]+ thbpt[c]
34HPLtm		h[c]+ 34hpl[c] <=> h[m]+ 34hpl[m]
4ABUTtm		4abut[c] <=> 4abut[m]
DAGK_hs		
AACOAT		
ABTArm		akg[m]+ 4abut[m] <=> glu_L[m]+ sucsal[m]
ABUTt2r	h[e]+ 4abut[e] <=> h[c]+ 4abut[c]	
ABUTt4_2_r	2 na1[e]+ 4abut[e] <=> 2 na1[c]+ 4abut[c]	
ACGLUtm		acglu[c] <=> acglu[m]
ACHEe		
ADK1m		atp[m]+ amp[m] <=> 2 adp[m]
AGTim		ala_L[m]+ glx[m] -> pyr[m]+ gly[m]
AKGDm		akg[m]+ coa[m]+ nad[m] -> co2[m]+ nadh[m]+ succoa[m]
AKGMALtm		akg[m]+ mal_L[c] <=> akg[c]+ mal_L[m]
ALAt2r		h[e]+ ala_L[e] <=> h[c]+ ala_L[c]

Reaction abbreviation	Reaction description	Reaction formula
ALOX5		
AMETt2m		amet[c]+ ahcys[m] <=> ahcys[c]+ amet[m]
APOC_LYS_BTNPm		h2o[m]+ apoC_Lys_btn[m] -> apoC[m]+ biocyt[m]
ARGNm		h2o[m]+ arg_L[m] -> urea[m]+ orn[m]
ASPGLUm		h[c]+ glu_L[c]+ asp_L[m] -> h[m]+ glu_L[m]+ asp_L[c]
ASPNATm		asp_L[m]+ accoa[m] -> h[m]+ coa[m]+ Nacasp[m]
ASPTAm		akg[m]+ asp_L[m] <=> glu_L[m]+ oaa[m]
ATPS4mi		4 h[c]+ adp[m]+ pi[m] -> 3 h[m]+ h2o[m]+ atp[m]
BDHm		nad[m]+ bhb[m] <=> h[m]+ nadh[m]+ acac[m]
C02712tm		C02712[c] <=> C02712[m]
C09642te		C09642[c] <=> C09642[e]
C160CPT1		
C160CPT2		coa[m]+ pmtcrn[m] -> crn[m]+ pmtcoa[m]
CATm		2 h2o2[m] -> o2[m]+ 2 h2o[m]
CHSTEROLt		h2o[c]+ atp[c]+ chsterol[c] -> adp[c]+ h[c]+ pi[c]+ chsterol[e]
CK		atp[m]+ creat[m] <=> adp[m]+ pcreat[m]
CKc		
CSm		h2o[m]+ accoa[m]+ oaa[m] -> h[m]+ coa[m]+ cit[m]
CSNAT2m		coa[m]+ pcrn[m] <=> ppcoa[m]+ crn[m]
CSNATm		coa[m]+ acrn[m] <=> accoa[m]+ crn[m]
CYOOm2i		o2[m]+ 4 focytC[m] -> 4 h[m]+ 2 h2o[m]+ 4 ficytC[m]
CYOOm3i		7.92 h[m]+ o2[m]+ 4 focytC[m] -> 1.96 h2o[m]+ 4 h[c]+ 4 ficytC[m]+ 0.02 o2s[m]
CYOR_u10mi		2 h[m]+ 2 ficytC[m]+ q10h2[m] -> 4 h[c]+ q10[m]+ 2 focytC[m]
DURIK1m		atp[m]+ duri[m] -> h[m]+ adp[m]+ dump[m]
ENO		
ETF		fadh2[m]+ etfox[m] -> fad[m]+ etfrd[m]
EX_4abut[e]		
EX_arachd[e]		
EX_atp[e]		
EX_bhb[e]		
EX_chsterol[e]		
EX_gln_L[e]		
EX_h[e]		
EX_h2o2[e]		
EX_hco3[e]		
EX_k[e]		
EX_lneldc[e]		
EX_lnlncg[e]		
EX_met_L[e]		

Reaction abbreviation	Reaction description	Reaction formula
EX_na1[e]		
EX_nh4[e]		
EX_pi[e]		
EX_strdnc[e]		
EX_thr_L[e]		
FADH2ETC		fadh2[m]+ q10[m] -> fad[m]+ q10h2[m]
FAOXC160		7 h2o[m]+ 7 coa[m]+ 7 nad[m]+ 7 fad[m]+ pmtcoa[m] -> 7 h[m]+ 7 nadh[m]+ 8 accoa[m]+ 7 fadh2[m]
FBA		
FE2DMT1		h[e]+ fe2[e] -> h[c]+ fe2[c]
FUMm		h2o[m]+ fum[m] <=> mal_L[m]
G3PD2m		fad[m]+ glyc3p[c] -> fadh2[m]+ dhap[c]
G6PDH2c		
G6PDH2r		
GAPD		
GBA		
GBA2e		
GLCt1r		
GLNtm		gln_L[c] -> gln_L[m]
GLUNm		h2o[m]+ gln_L[m] -> glu_L[m]+ nh4[m]
GLUt2m		h[c]+ glu_L[c] <=> h[m]+ glu_L[m]
GLUVESSEC		
GLYKm		atp[m]+ glyc[m] -> h[m]+ adp[m]+ glyc3p[m]
GND		
GNDc		
GTHO		
GTHOm		h[m]+ nadph[m]+ gthox[m] -> nadp[m]+ 2 gthrd[m]
GTHP		
GTHPm		h2o2[m]+ 2 gthrd[m] -> 2 h2o[m]+ gthox[m]
H2CO3Dm		h2o[m]+ co2[m] -> h[m]+ hco3[m]
H2O2tm		h2o2[c] -> h2o2[m]
H2OGLYAQPt	h2o[e]+ glyc[e] <=> h2o[c]+ glyc[c]	
HEX1		
HISTAtu	hista[e] <=> hista[c]	
Htmi		h[c] -> h[m]
ICDHxm		nad[m]+ icit[m] -> akg[m]+ co2[m]+ nadh[m]
ICDHy		
ICDHyrm		nadp[m]+ icit[m] <=> nadph[m]+ akg[m]+ co2[m]
L_LACt2r		
L_LACtcm		lac_L[c] -> lac_L[m]

Reaction abbreviation	Reaction description	Reaction formula
LDH_L		
LDH_Lm		nad[m]+ lac_L[m] <=> h[m]+ nadh[m]+ pyr[m]
LGTHL		
LNSTLSr		
MDH		
MDHm		nad[m]+ mal_L[m] <=> h[m]+ nadh[m]+ oaa[m]
ME2m		nadp[m]+ mal_L[m] -> nadph[m]+ co2[m]+ pyr[m]
MTHFD2m		nad[m]+ mlthf[m] <=> nadh[m]+ methf[m]
NADH2_u10mi		5 h[m]+ nadh[m]+ q10[m] -> 4 h[c]+ nad[m]+ q10h2[m]
NMNATn		
OCOAT1m		acac[m]+ succoa[m] -> aacoa[m]+ succ[m]
ORNtiDF		orn[e] -> orn[c]
P45011A1m		h[m]+ nadph[m]+ 2 o2[m]+ chsterol[m] -> 2 h2o[m]+ nadp[m]+ 4mptnl[m]+ prgnlone[m]
P45027A11m		h[m]+ nadph[m]+ o2[m]+ xoltriol[m] -> h2o[m]+ nadp[m]+ xoltetrol[m]
P45027A12m		nadp[m]+ xoltetrol[m] -> h[m]+ nadph[m]+ thcholst[m]
P45027A13m		nadph[m]+ o2[m]+ thcholst[m] -> h2o[m]+ nadp[m]+ thcholstoic[m]
P45027A14m		h[m]+ nadph[m]+ o2[m]+ xol7ah2[m] -> h2o[m]+ nadp[m]+ xol7ah3[m]
P45027A15m		h[m]+ nadph[m]+ o2[m]+ xol7ah3[m] -> 2 h2o[m]+ nadp[m]+ xol7ah2al[m]
P45027A16m		nadph[m]+ o2[m]+ xol7ah2al[m] -> h2o[m]+ nadp[m]+ dhcholestanate[m]
P45027A1m		h[m]+ nadph[m]+ o2[m]+ chsterol[m] -> h2o[m]+ nadp[m]+ xol27oh[m]
PDHm		coa[m]+ nad[m]+ pyr[m] -> co2[m]+ nadh[m]+ accoa[m]
PEFLIPm		h2o[c]+ atp[c]+ pe_hs[c] -> adp[c]+ h[c]+ pi[c]+ pe_hs[m]
PETOHMm_hs		3 amet[m]+ pe_hs[m] -> 3 h[m]+ 3 ahcys[m]+ pchol_hs[m]
PFK		
PGI		
PGK		
PGL		
PGLc		
PGM		
PPM		
PSDm_hs		h[m]+ ps_hs[m] -> co2[m]+ pe_hs[m]
PYK		
r0022		nad[m]+ 2 gthrd[m] <=> h[m]+ nadh[m]+ gthox[m]
r0081		akg[m]+ ala_L[m] <=> glu_L[m]+ pyr[m]
r0083		h[m]+ HC01434[m] -> akg[m]+ co2[m]
r0321		coa[m]+ acac[m]+ atp[m] -> aacoa[m]+ amp[m]+ ppi[m]
r0399		

Reaction abbreviation	Reaction description	Reaction formula
r0407		
r0408		
r0409		
r0423		nadp[m]+ icit[m] -> h[m]+ nadph[m]+ HC01434[m]
r0425		nad[m]+ icit[m] <=> h[m]+ nadh[m]+ HC01434[m]
r2535m		hom_L[m] <=> hom_L[c]
r2539		L2aadp[m]+ L2aadp6sa[c] <=> L2aadp[c]+ L2aadp6sa[m]
RBK		
RBK_D		
RE0124C		
RE1530M		dgtp[m]+ duri[m] <=> h[m]+ dgdp[m]+ dump[m]
RE1804M		nad[m]+ xol7ah3[m] <=> h[m]+ nadh[m]+ xol7ah2al[m]
RE1807M		h2o[m]+ nadp[m]+ xol7ah2al[m] <=> 2 h[m]+ nadph[m]+ dhcholestanate[m]
RE2625M		nad[m]+ xoltetrol[m] <=> h[m]+ nadh[m]+ CE4872[m]
RE2626M		h2o[m]+ nadp[m]+ CE4872[m] <=> 2 h[m]+ nadph[m]+ thcholstoic[m]
RE3251M		h[m]+ nadph[m]+ o2[m]+ xoltetrol[m] -> h2o[m]+ nadp[m]+ CE4874[m]
RPE		
RPEc		
RPI		
SARDHm		fad[m]+ sarcs[m]+ thf[m] -> fadh2[m]+ gly[m]+ mlthf[m]
SPODMm		2 h[m]+ 2 o2s[m] -> o2[m]+ h2o2[m]
SRTNtu	srtn[e] <=> srtn[c]	
STS1		
SUCD1m		fad[m]+ succ[m] <=> fadh2[m]+ fum[m]
SUCOASm		coa[m]+ atp[m]+ succ[m] <=> adp[m]+ pi[m]+ succoa[m]
TALA		
TAUPAT1c	h[e]+ taur[e] -> h[c]+ taur[c]	
TKT1		
TKT2		
TMDK1m		atp[m]+ thymd[m] -> h[m]+ adp[m]+ dtmp[m]
DM_atp_c_ DM_4glu56dihdi nd[c]	4-S-Glutathionyl-5,6-Dihydroxyindoline	
DM_CE5025[c]	5-S-Glutathionyl-Dopamine	
DM_CE5026[c]	5-S-Glutathionyl-L-Dopa	
DM_CE1562[c]	5,6-Indolequinone-2-Carboxylate	
DM_ind56qn[c]	Indole-5,6-Quinone	
DM_ascb_L[c]	L-Ascorbate	
sink_asn_L[c]	L-Asparagine	

Reaction abbreviation	Reaction description	Reaction formula
DM_no2[c]	Nitrite	
sink_thmtp[c]	Thiamine-Triphosphate	
DM_6hddopaqn[c]	6-Hydroxydopamine-Quinone	
sink_chol[c]	Choline	
DM_CE4888[c]	Dopaminochrome	
DM_gm1_hs[n]	Ganglioside Gm1	
sink_pre_prot[r]	Glycophosphatidylinositol (Gpi)-Anchored Protein Precursor	
sink_fe3[c]	Iron (Fe3+)	
sink_citr[c]	L-Citrulline	
sink_lnlc[c]	Linoleate	
sink_lnlccoa[c]	Linoleic Coenzyme A	
DM_C02712[c]	N-Acetylmethionine	
sink_nadp[c]	Nicotinamide Adenine Dinucleotide Phosphate	
sink_nad[c]	Nicotinamide Adenine Dinucleotide	
sink_odecoa[c]	Octadecenoyl Coenzyme A (N-C18:1 Coenzyme A)	
sink_pmtcoa[c]	Palmitoyl Coenzyme A (N-C16:0 Coenzyme A)	
DM_pchol_hs[c]	Phosphatidylcholine	
DM_pcreat[c]	Phosphocreatine	
sink_phyQ[c]	Phylloquinone	
DM_K_c_	Potassium	
DM_Ser_Gly_Ala_X_Gly_ly_	Protein-Linked Serine Residue (Glycosaminoglycan Attachment Site)	
sink_Ser_Gly_Ala_X_Gly[r]	Protein-Linked Serine Residue (Glycosaminoglycan Attachment Site)	
DM_na1[c]	Sodium	
DM_sprm_c_	Spermine	
sink_stcoa[c]	Stearoyl Coenzyme A (N-C18:0 Coenzyme A)	
DM_taur[c]	Taurine	
DM_thm[m]	Thiamin	
sink_thmpp[c]	Thiamine Diphosphate	
sink_Tyr_ggn[c]	Tyr-194 Of Apo-Glycogenin Protein (Primer For Glycogen Synthesis)	
DM_ca2[c]	Calcium	
DM_chsterol[c]	cholesterol	
DM_pnto_R	(R)-Pantothenate	
DM_CE1261[c]	5-S-Cysteinyldopa	
sink_CE1273[c]	5Beta-Cholestane-3Alpha,7Alpha,12Alpha,24S,25-Pentol	
sink_crvnc[c]	Cervonic Acid, C22:6 N-3	
sink_decdicoa[c]	Decadienoyl Coenzyme A	
sink_c101coa[c]	Decenoyl Coenzyme A	
DM_pail35p_hs[n]	1-Phosphatidyl-1D-Myo-Inositol 3,5-Bisphosphate	

Reaction abbreviation	Reaction description	Reaction formula
DM_5cysdopa[c]	5-S-Cysteinyldopamine	
sink_retfa[c]	Fatty Acid Retinol	
HMR_1735		o2[c]+ h[c]+ nadph[c]+ chsterol[c] -> h2o[c]+ nadp[c]+ xol24oh[c]
CLS_hs		cdpdag_hs[c]+ pglyc_hs[c] -> h[c]+ cmp[c]+ clpn_hs[c]
PIK4		atp[c]+ pail_hs[c] -> h[c]+ adp[c]+ pail4p_hs[c]
PSDm_hs		h[m]+ ps_hs[m]-> co2[m]+ pe_hs[m]
HMR_0653		amet[c]+ pe_hs[c] -> 2 h[c]+ ahcys[c]+ M02686[c]
PCHOLP_hs		h2o[c]+ pchol_hs[c] -> h[c]+ pa_hs[c]+ chol[c]
PLA2_2		h2o[c]+ pchol_hs[c] -> h[c]+ Rtotal2[c]+ lpchol_hs[c]
SMS		pchol_hs[c]+ crm_hs[c] -> dag_hs[c]+ sphmyln_hs[c]
HMR_0795		h2o[c]+ sphmyln_hs[c] -> h[c]+ crm_hs[c]+ cholp[c]
NTD4		h2o[c]+ cmp[c] -> pi[c]+ cytd[c]
AMPDA		h2o[c]+ h[c]+ amp[c] -> nh4[c]+ imp[c]
NTD7		h2o[c]+ amp[c] -> pi[c]+ adn[c]
NTD9		h2o[c]+ gmp[c] -> pi[c]+ gsn[c]
NTD2		h2o[c]+ ump[c] -> pi[c]+ uri[c]
ASPTA		akg[c]+ asp_L[c] <=> glu_L[c]+ oaa[c]
FPGS2		atp[c]+ glu_L[c]+ 5thf[c] -> h[c]+ adp[c]+ pi[c]+ 6thf[c]
FPGS3		atp[c]+ glu_L[c]+ 6thf[c] -> h[c]+ adp[c]+ pi[c]+ 7thf[c]
FPGS4		atp[c]+ 4 glu_L[c]+ dhf[c] -> 3 h2o[c]+ h[c]+ adp[c]+ pi[c]+ 5dhf[c]
FPGS5		atp[c]+ glu_L[c]+ 5dhf[c] -> h[c]+ adp[c]+ pi[c]+ 6dhf[c]
FPGS6		atp[c]+ glu_L[c]+ 6dhf[c] -> h[c]+ adp[c]+ pi[c]+ 7dhf[c]
FPGS8		10fthf5glu[c]+ atp[c]+ glu_L[c] -> 10fthf6glu[c]+ h[c]+ adp[c]+ pi[c]
FPGS9		10fthf6glu[c]+ atp[c]+ glu_L[c] -> 10fthf7glu[c]+ h[c]+ adp[c]+ pi[c]
r1382		6 atp[c]+ 6 glu_L[c]+ thf[c] -> 6 h[c]+ 6 adp[c]+ 6 pi[c]+ 7thf[c]
FPGS7		10fthf[c]+ atp[c]+ 4 glu_L[c] -> 10fthf5glu[c]+ 3 h2o[c]+ h[c]+ adp[c]+ pi[c]
FPGS		atp[c]+ 4 glu_L[c]+ thf[c] -> 3 h2o[c]+ h[c]+ adp[c]+ pi[c]+ 5thf[c]
HMR_9726		glu_L[c]+ 5fthf[c] -> thf[c]+ forglu[c]
ALATA_L		akg[c]+ ala_L[c] <=> pyr[c]+ glu_L[c]
GLUCYS		atp[c]+ glu_L[c]+ cys_L[c] -> h[c]+ adp[c]+ pi[c]+ glucys[c]
ILETA		akg[c]+ ile_L[c] <=> glu_L[c]+ 3mop[c]
LEUTA		akg[c]+ leu_L[c] <=> glu_L[c]+ 4mop[c]
VALTA		akg[c]+ val_L[c] <=> glu_L[c]+ 3mob[c]
ARGSS		atp[c]+ asp_L[c]+ citr_L[c] -> h[c]+ amp[c]+ ppi[c]+ argsuc[c]
ASPTA		akg[c]+ asp_L[c] <=> glu_L[c]+ oaa[c]
ALATA_L		akg[c]+ ala_L[c] <=> pyr[c]+ glu_L[c]
GHMT2r		ser_L[c]+ thf[c] <=> h2o[c]+ gly[c]+ mlthf[c]
GLYAMDTRc		gly[c]+ arg_L[c] <=> orn[c]+ gudac[c]

Reaction abbreviation	Reaction description	Reaction formula
r0060		ser_L[c] -> nh4[c]+ pyr[c]
THRD_L		thr_L[c] -> nh4[c]+ 2obut[c]
GHMT2r		ser_L[c]+ thf[c] <=> h2o[c]+ gly[c]+ mlthf[c]
GLYAMDTRc		gly[c]+ arg_L[c] <=> orn[c]+ gudac[c]
ARGN		h2o[c]+ arg_L[c] -> orn[c]+ urea[c]
r0145		2 o2[c]+ 2 nadph[c]+ arg_L[c] -> 2 h2o[c]+ 2 nadp[c]+ citr_L[c]+ no[c]
THRD_L		thr_L[c] -> nh4[c]+ 2obut[c]
PHETHPTOX2		o2[c]+ thbpt[c]+ phe_L[c] -> tyr_L[c]+ thbpt4acam[c]
PROD2		fad[c]+ pro_L[c] -> h[c]+ fadh2[c]+ 1pyr5c[c]
HMR_6728		o2[c]+ thbpt[c]+ tyr_L[c] -> h2o[c]+ 34dhphe[c]+ dhbpt[c]
HMR_6874		o2[c]+ tyr_L[c] -> h2o[c]+ dopaqn[c]
TYR3MO2		o2[c]+ thbpt[c]+ tyr_L[c] -> 34dhphe[c]+ thbpt4acam[c]
TYRCBOX		h[c]+ tyr_L[c] -> co2[c]+ tym[c]
TYRTA		akg[c]+ tyr_L[c] <=> 34hpp[c]+ glu_L[c]
LYSOXp		
HISDC		h[c]+ his_L[c] -> co2[c]+ hista[c]
HISD		his_L[c] -> nh4[c]+ urcan[c]
LEUTA		akg[c]+ leu_L[c] <=> glu_L[c]+ 4mop[c]
ILETA		akg[c]+ ile_L[c] <=> glu_L[c]+ 3mop[c]
VALTA		akg[c]+ val_L[c] <=> glu_L[c]+ 3mob[c]
METAT		h2o[c]+ atp[c]+ met_L[c] -> pi[c]+ amet[c]+ ppi[c]
GLUDxm	glutamate dehydrogenase (NAD) (mitochondrial)	h2o[m]+ nad[m]+ glu_L[m]<=> h[m]+ akg[m]+ nadh[m]+ nh4[m]
GLUDym	glutamate dehydrogenase (NADP), mitochondrial	h2o[m]+ nadp[m]+ glu_L[m]<=> h[m]+ nadph[m]+ akg[m]+ nh4[m]
ACONTm		
r0426		
r1109		
MTHFR3		
METS		
DOPAOQNOX		

Table S3. List of metabolites predicted to be secreted along with their psychochemical nature and biological class.

Recon3D Names	Hydrophobicity	Chemical Class
Lipoamide	Apolar / hydrophobic	Lipoamide
17beta-hydroxy-5alpha-androstan-3-one	Apolar / hydrophobic	Steroid
Dolichol	Apolar / hydrophobic	Polyprenol
Lanosterin	Apolar / hydrophobic	Sterol
Bilirubin	Predicted informative metabolites	Bilirubin
Thromboxane A2	Apolar / hydrophobic	Eicosanoid
Retinoyl b-glucuronide	Apolar / hydrophobic	Terpene glycoside
21-Hydroxypregnenolone	Apolar / hydrophobic	Steroid
7-a,27-Dihydroxycholesterol	Apolar / hydrophobic	Bile acid
(24S)-7Alpha,24-Dihydroxycholesterol	Apolar / hydrophobic	Bile acid
Hexanoyl-CoA	Apolar / hydrophobic	Fatty acyl Coenzyme
Ceramide 1-Phosphate	Apolar / hydrophobic	Sphingolipid
Stearidonic acid	Apolar / hydrophobic	Fatty acid
12,13-DHOME	Apolar / hydrophobic	Fatty acid
24-Hydroxycholesterol	Apolar / hydrophobic	Sterol
Cholesterol	Apolar / hydrophobic	Sterol
Cholesterol ester	Apolar / hydrophobic	Sterol
Gamma-Linolenic acid	Apolar / hydrophobic	Fatty acid
Vitamin K1	Apolar / hydrophobic	Prenol Lipid
Sphinganine 1-phosphate	Apolar / hydrophobic	Sphingolipid
Cholestane-3,7,12,24,25-pentol	Apolar / hydrophobic	Sterol
7Z,10Z-Hexadecadienoic Acid	Apolar / hydrophobic	Fatty acid
Linoelaidic Acid (All Trans C18:2)	Apolar / hydrophobic	Fatty acid
13-cis-Retinoic acid	Apolar / hydrophobic	Prenol lipid
Retinal	Apolar / hydrophobic	Prenol Lipid
5-Amino-1-(5-Phospho-D-ribosyl)imidazole-4-carboxamide	Polar / hydrophilic	Nucleotide
5-Methylthioadenosine	Polar / hydrophilic	Nucleoside
S-Adenosyl-L-homocysteine	Polar / hydrophilic	Nucleoside
Urocanate	Polar / hydrophilic	Imidazoyl carboxylic acid

Recon3D Names	Hydrophobicity	Chemical Class
Kynurenate	Polar / hydrophilic	Quinoline carboxylic acid
2-Oxobutanoate	Polar / hydrophilic	Keto acid
2-Oxoadipate(2-)	Polar / hydrophilic	Keto acid
Leucylleucine	Polar / hydrophilic	Dipeptide
Dehydroascorbic acid	Polar / hydrophilic	Sugar acid
4-Acetamidobutanoic acid	Polar / hydrophilic	Amino acid
Lactose	Polar / hydrophilic	Sugar
D-Xylose	Polar / hydrophilic	Sugar
D-Iduronic acid	Polar / hydrophilic	Sugar acid
4-Methylpentanal	Polar / hydrophilic	Aldehyde
D-Glucuronic acid	Polar / hydrophilic	Sugar acid
Orotidylic acid	Polar / hydrophilic	Nucleotide
Galactose	Polar / hydrophilic	Sugar
Adenosine triphosphate	Polar / hydrophilic	Nucleotide
N-Acetylmannosamine	Polar / hydrophilic	Amino sugar
Isomaltose	Polar / hydrophilic	Sugar
Nicotinic acid mononucleotide	Polar / hydrophilic	Nucleotide
N-Acetyl-L-aspartic acid	Polar / hydrophilic	Amino acid
N-Acetylglutamic acid	Polar / hydrophilic	Amino acid
1-Methylnicotinamide	Polar / hydrophilic	Nicotinamide
Tetrahydrobiopterin	Polar / hydrophilic	Pterin
D-Gluconate	Polar / hydrophilic	Sugar acid
Inosine	Polar / hydrophilic	Nucleoside
Xanthine	Polar / hydrophilic	Nucleobase
Alpha-D-Glucose 1,6-bisphosphate	Polar / hydrophilic	Sugar phosphate
1,5-D-Gluconolactone	Polar / hydrophilic	Sugar lactone
2-Methyl-3-Hydroxy-Valerate	Polar / hydrophilic	Carboxylic acid
Hydroxytyrosol	Polar / hydrophilic	Phenyl alcohol

Supplementary References

1. Inglis A.S. and Teh-Yung Liu. “The Stability of Cysteine and Cystine during Acid Hydrolysis of Proteins and Peptides”. In: *The Journal of Biological Chemistry* 245.1 (1970), pp. 112–116. url: http://w/ww.jbc.org/content/245/1/112 (visited on 04/13/2018).
2. Linda Ahonen et al. “Analysis of Oxysterols and Vitamin D Metabolites in Mouse Brain and Cell Line Samples by Ultra-High-Performance Liquid Chromatography-Atmospheric Pressure Photoionization–MassSpectrometry”.In: *Journal of Chromatography A* 1364(Oct.2014),pp.214– 222. doi: 10.1016/j.chroma.2014.08.088. pmid: 25204266.
3. Rodrigo D. A. M. Alvesetal. “Global Profiling of the Muscle Metabolome : Method Optimization, Validation and Application to Determine Exercise-Induced Metabolic Effects”. In: *Metabolomics* 11.2 (Apr. 1, 2015), pp. 271–285. doi: 10.1007/s11306-014-0701-7.
4. Maike K. Aurich, Ronan M. T. Fleming, and Ines Thiele. “MetaboTools: A Comprehensive Toolbox for Analysis of Genome-Scale Metabolic Models”. In: *Frontiers in Physiology* 7 (2016). doi: 10.3389/fphys.2016.00327.
5. M. Banay-Schwartz et al. “Protein Content of Various Regions of Rat Brain and Adult and Aging Human Brain”. In: *AGE* 15.2 (Apr. 1, 1992), pp. 51–54. doi: 10.1007/BF02435024.
6. O. Begou et al. “Hyphenated MS-Based Targeted Approaches in Metabolomics”. In: *The Analyst* 2011 (2017), pp. 3079–3100. doi: 10.1039/C7AN00812K. pmid: 28792021.
7. Elizabeth Brunketal. “Recon3D Enables a Three-Dimensional View of Gene Variation in Human Metabolism”. In: *Nature Biotechnology* 36 (Feb. 19, 2018), p. 272. url: http://dx.doi.org/ 10.1038/nbt.4072.
8. Tomas Cajka and Oliver Fiehn. “Comprehensive Analysis of Lipids in Biological Systems by Liquid Chromatography-Mass Spectrometry”. In: *TrAC Trends in Analytical Chemistry* 61 (Oct. 2014), pp. 192–206. doi: 10.1016/j.trac.2014.04.017. pmid: 25309011.
9. Tomas Cajka, Jennifer T. Smilowitz, and Oliver Fiehn. “Validating Quantitative Untargeted LipidomicsAcrossNineLiquidChromatography–High ResolutionMassSpectrometryPlatforms”. In: *Analytical Chemistry* 89.22 (Nov.

2017), pp. 12360–12368. doi: 10.1021/acs.analchem. 7b03404. pmid: 29064229.

10. AlexiesDagnino-Subiabreetal."Glutathione Transferase M22 Catalyzes Conjugation of Dopamine and Dopa o-Quinones". In: *Biochemical and Biophysical Research Communications* 274.1 (July 21, 2000), pp. 32–36. doi: 10.1006/bbrc.2000.3087.
11. Carola W. N. Damen et al. "Enhanced Lipid Isomer Separation in Human Plasma Using Reversed-Phase UPLC with Ion-Mobility/High-Resolution MS Detection". In: *Journal of Lipid Research* 55.8 (Aug. 2014), pp. 1772–1783. doi: 10.1194/jlr.D047795. pmid: 24891331.
12. F. Diego et al. "Automated Identification of Neuronal Activity from Calcium Imaging by Sparse Dictionary Learning". In: *2013 IEEE 10th International Symposium on Biomedical Imaging (ISBI)*. 2013 IEEE 10th International Symposium on Biomedical Imaging (ISBI). Apr. 2013, pp. 1058–1061. doi: 10.1109/ISBI.2013.6556660.
13. Arthur Edelstein et al. "Computer Control of Microscopes Using μManager". In: *Current Protocols in Molecular Biology*. John Wiley & Sons, Inc., 2001. url: http://onlinelibrary.wiley. com/doi/10.1002/0471142727.mb1420s92/abstract (visited on 04/14/2015).
14. Graeme Eisenhofer, Irwin J. Kopin, and David S. Goldstein. "Catecholamine Metabolism: A Contemporary View with Implications for Physiology and Medicine". In: *Pharmacological Reviews* 56.3 (Jan. 9, 2004), pp. 331–349. doi: 10.1124/pr.56.3.1. pmid: 15317907.
15. Adam M Feist and Bernhard O Palsson. "The Biomass Objective Function". In: *Current Opinion in Microbiology*. Ecology and Industrial Microbiology • Special Section: Systems Biology 13.3 (June 2010), pp. 344–349. doi: 10.1016/j.mib.2010.03.003.
16. Junzeng Fu et al. "Metabolomics Profiling of the Free and Total Oxidised Lipids in Urine by LCMS/MS: Application in Patients with Rheumatoid Arthritis". In: *Analytical and Bioanalytical Chemistry* 408.23 (2016), pp. 6307–6319. doi: 10.1007/s00216-016-9742-2. pmid: 27405874.
17. Juan C. García-Cañaveras et al. "Targeted Profiling of Circulating and Hepatic Bile Acids in Human, Mouse, and Rat Using a UPLC-MRM-MS-Validated

Method". In: *Journal of Lipid Research* 53.10 (2012), pp. 2231–2241. doi: 10.1194/jlr.D028803. pmid: 22822028.

18. Teresa A. Garrett, Ziqiang Guan, and Christian R H Raetz. "Analysis of Ubiquinones, Dolichols, and Dolichol Diphosphate-Oligosaccharides by Liquid Chromatography-Electrospray IonizationMass Spectrometry". In: *Methods in Enzymology* 432.07 (2007), pp. 117–143. doi: 10.1016/ S0076-6879(07)32005-3. pmid: 17954215.
19. Helen G. Gika et al. "Quantitative Profiling of Polar Primary Metabolites Using Hydrophilic Interaction Ultrahigh Performance Liquid Chromatography-Tandem Mass Spectrometry". In: *Journal of Chromatography A* 1259 (2012), pp. 121–127. doi: 10.1016/j.chroma.2012.02.010. pmid: 22381888.
20. Nicola Gray et al. "High-Speed Quantitative UPLC-MS Analysis of Multiple Amines in Human PlasmaandSerumviaPrecolumnDerivatizationwith6-Aminoquinolyl-N-Hydroxysuccinimidyl Carbamate: Application to Acetaminophen-Induced Liver Failure". In: *Analytical Chemistry* 89.4 (Feb. 2017), pp. 2478–2487. doi: 10.1021/acs.analchem.6b04623. pmid: 28194962.
21. Steinn Gudmundsson and Ines Thiele. "Computationally Efficient Flux Variability Analysis". In: *BMC Bioinformatics* 11.1 (Sept. 29, 2010), p. 489. doi: 10.1186/1471-2105-11-489.
22. Jennifer Haggarty and Karl EV Burgess. "Recent Advances in Liquid and Gas Chromatography Methodology for Extending Coverage of the Metabolome". In: *Current Opinion in Biotechnology* 43 (2017), pp. 77–85. doi: 10.1016/j.copbio.2016.09.006. pmid: 27771607.
23. J. A. Hanley and B. J. McNeil. "The Meaning and Use of the Area under a Receiver Operating Characteristic (ROC) Curve". In: *Radiology* 143.1 (Apr. 1982), pp. 29–36. doi: 10.1148/ radiology.143.1.7063747. pmid: 7063747.
24. Hulda S. Haraldsdóttir and Ronan M. T. Fleming. "Identification of Conserved Moieties in Metabolic Networks by Graph Theoretical Analysis of Atom Transition Networks". In: *PLOS Computational Biology* 12.11 (Nov. 21, 2016), e1004999. doi: 10.1371/journal.pcbi.1004999.

25. Hulda S. Haraldsdóttir et al. “CHRR: Coordinate Hit-and-Run with Rounding for Uniform Sampling of Constraint-Based Models”. In: *Bioinformatics* 33.11 (Jan. 6, 2017), pp. 1741–1743. doi: 10.1093/bioinformatics/btx052.
26. Laurent Heirendt et al. “Creation and Analysis of Biochemical Constraint-Based Models: The COBRA Toolbox v3.0”. In: *Nature Protocols (accepted)* (2018). url: https://arxiv.org/abs/ 1710.04038 (visited on 07/28/2017).
27. Katriina Itäaho et al. “Dopamine Is a Low-Affinity and High-Specificity Substrate for the Human UDP-Glucuronosyltransferase 1A10”. In: *Drug Metabolism and Disposition* 37.4 (Jan. 4, 2009), pp. 768–775. doi: 10.1124/dmd.108.025692. pmid: 19116261.
28. Gregory Kapatos. “The Neurobiology of Tetrahydrobiopterin Biosynthesis: A Model for Regulation of GTP Cyclohydrolase I Gene Transcription within Nigrostriatal Dopamine Neurons”. In: *IUBMB Life* 65.4 (Apr. 1, 2013), pp. 323–333. doi: 10.1002/iub.1140.
29. Hiroko Kato et al. “Widely Targeted Metabolic Profiling Analysis of Yeast Central Metabolites”. In: *Journal of Bioscience and Bioengineering* 113.5 (May 2012), pp. 665–673. doi: 10.1016/j. jbiosc.2011.12.013. pmid: 22280965.
30. Daehwan Kim et al. “TopHat2: Accurate Alignment of Transcriptomes in the Presence of Insertions, Deletions and Gene Fusions”. In: *Genome Biology* 14.4 (2013), R36. doi: 10.1186/gb2013-14-4-r36. pmid: 23618408.
31. Hee-Yong Kim, Bill X. Huang, and Arthur A. Spector. “Phosphatidylserine in the Brain: Metabolism and Function”. In: *Progress in lipid research* 0 (Oct. 2014), pp. 1–18. doi: 10.1016/j. plipres.2014.06.002. pmid: 24992464.
32. Maud M Koek et al. “Microbial Metabolomics with Gas Chromatography/Mass Spectrometry.” In: *Analytical Chemistry* 78.4 (Feb. 2006), pp. 1272–81. doi: 10.1021/ac051683+. pmid: 16478122.
33. Michael J. Kuhar. “On the Use of Protein Turnover and Half-Lives”. In: *Neuropsychopharmacology* 34.5 (Oct. 15, 2008), pp. 1172–1173. doi: 10.1038/npp.2008.190.
34. Petri Kylli, Thomas Hankemeier, and Risto Kostiainen. “Feasibility of Ultra-Performance Liquid Chromatography–Ion Mobility–Time-of-Flight Mass Spectrometry in Analyzing Oxysterols”. In: *Journal of Chromatography A* 1487 (2017), pp. 147–152. doi: 10.1016/j.chroma.2017.01.039.

35. Ruth Landolt, Helen H. Hess, and Caroline Thalheimer. “Regional Distribution of Some Chemical Structural Components of the Human Nervous System—I”. In: *Journal of Neurochemistry* 13.12 (Dec. 1, 1966), pp. 1441–1452. doi: 10.1111/j.1471-4159.1966.tb04305.x.
36. Heng Li et al. “The Sequence Alignment/Map Format and SAMtools”. In: *Bioinformatics* 25.16 (Aug. 15, 2009), pp. 2078–2079. doi: 10.1093/bioinformatics/btp352. pmid: 19505943.
37. Gerhard Liebisch et al. “High Throughput Quantification of Cholesterol and Cholesteryl Ester by Electrospray Ionization Tandem Mass Spectrometry (ESI-MS/MS)”. In: *Biochimica et Biophysica Acta - Molecular and Cell Biology of Lipids* 1761.1 (2006), pp. 121–128. doi: 10.1016/ j.bbalip.2005.12.007.
38. R. Mahadevan and C. H. Schilling. “The Effects of Alternate Optimal Solutions in ConstraintBased Genome-Scale Metabolic Models”. In: *Metabolic Engineering* 5.4 (Oct. 2003), pp. 264–276.doi: 10.1016/j.ymben.2003.09.002.
39. MarcelMartin.“CutadaptRemovesAdapterSequencesfromHigh-ThroughputSequencingReads”. In: *EMBnet.journal* 17.1 (May 2, 2011), pp. 10-12. doi: 10.14806/ej.17.1.200.
40. C. A. Mawson. “Meaning of ‘Turnover’ in Biochemistry”. In: *Nature* 176.4476 (Aug. 13, 1955), pp. 317–317. doi: 10.1038/176317a0.
41. Johannes Meiser, Daniel Weindl, and Karsten Hiller. “Complexity of Dopamine Metabolism”. In: *Cell Communication and Signaling : CCS* 11 (May 17, 2013), p. 34. doi: 10.1186/1478811X-11-34.
42. Alfred H. Merrill et al. “Sphingolipidomics: High-Throughput, Structure-Specific, and Quantitative Analysis of Sphingolipids by Liquid Chromatography Tandem Mass Spectrometry”. In: *Methods* 36 (2 SPEC. ISS. 2005), pp. 207–224. doi: 10.1016/j.ymeth.2005.01.009. pmid: 15894491.
43. Patricia Muñoz et al. “Dopamine Oxidation and Autophagy”. In: *Parkinson’s Disease* 2012 (2012). doi: 10.1155/2012/920953.
44. A. Napolitano, P. Manini, and M. d’Ischia. “Oxidation Chemistry of Catecholamines and Neuronal Degeneration: An Update”. In: *Current Medicinal Chemistry* 18.12 (2011), pp. 1832–1845. pmid: 21466469.
45. Alessandra Napolitano, Alessandro Pezzella, and Giuseppe Prota. “New Reaction Pathways of Dopamine under Oxidative Stress Conditions: Nonenzymatic Iron-Assisted Conversion to Norepinephrine and the

Neurotoxins 6-Hydroxydopamine and 6,7-Dihydroxytetrahydroisoquinoline". In: *Chemical Research in Toxicology* 12.11 (Nov. 1, 1999), pp. 1090–1097. doi: 10.1021/ tx990079p.

46. Marek J. Noga et al. "Metabolomics of Cerebrospinal Fluid Reveals Changes in the Central Nervous System Metabolism in a Rat Model of Multiple Sclerosis". In: *Metabolomics* 8.2 (Apr. 2011), pp. 253–263. doi: 10.1007/s11306-011-0306-3.
47. Alberto Noronha et al. "The Virtual Metabolic Human Database: A Comprehensive Metabolic Resource of Human and Human Associated Microbes." In: *In preparation* (2016).
48. William T. Norton et al. "The Lipid Composition of Isolated Brain Cells and Axons". In: *Journal of Neuroscience Research* 1.1 (Jan. 1, 1975), pp. 57–75. doi: 10.1002/jnr.490010106.
49. John S. O'Brien and E. Lois Sampson. "Lipid Composition of the Normal Human Brain: Gray Matter, White Matter, and Myelin". In: *Journal of Lipid Research* 6.4 (Jan. 10, 1965), pp. 537– 544. pmid: 5865382. url: http://w/ww.jlr.org/content/6/4/537 (visited on 08/12/2014).
50. G. Paglia et al. "Monitoring Metabolites Consumption and Secretion in Cultured Cells Using Ultra-Performance Liquid Chromatography Quadrupole-Time of Flight Mass Spectrometry (UPLC-Q-ToF-MS)." In: *Analytical and Bioanalytical Chemistry* 402.3 (2012), pp. 1183–98. doi: 10.1007/s00216-011-5556-4. pmid: 22159369.
51. Leslie B. Poole. "The Basics of Thiols and Cysteines in Redox Biology and Chemistry". In: *Free Radical Biology & Medicine* 80 (Mar. 2015), pp. 148–157. doi: 10.1016/j.freeradbiomed. 2014.11.013. pmid: 25433365.
52. German A. Preciat Gonzalez et al. "Comparative Evaluation of Atom Mapping Algorithms for Balanced Metabolic Reactions: Application to Recon3D". In: *Journal of Cheminformatics* 9 (2017), p. 39. doi: 10.1186/s13321-017-0223-1.
53. Syed Asad Rahman et al. "Reaction Decoder Tool (RDT): Extracting Features from Chemical Reactions".In: *Bioinformatics* 32.13(Jan.7,2016),pp.2065–2066. doi:10.1093/bioinformatics/ btw096. pmid: 27153692.
54. Peter Reinhardt et al. "Derivation and Expansion Using Only Small Molecules of Human Neural Progenitors for Neurodegenerative Disease Modeling". In:

PLoS ONE 8.3 (Mar. 22, 2013). Ed. by Marcel Daadi, e59252. doi: 10.1371/journal.pone.0059252.

55. KoenSandraetal."ComprehensiveBloodPlasmaLipidomicsbyLiquidChromatography/Quadrupole Time-of-Flight Mass Spectrometry". In: *Journal of Chromatography A* 1217.25 (June 2010), pp. 4087–4099. doi: 10.1016/j.chroma.2010.02.039. pmid: 20307888.
56. Augustin Scalbert et al. "Mass-Spectrometry-Based Metabolomics: Limitations and Recommendations for Future Progress with Particular Focus on Nutrition Research". In: *Metabolomics* 5.4 (Dec. 2009), pp. 435–458. doi: 10.1007/s11306-009-0168-0. pmid: 20046865.
57. Jan Schellenberger et al. "Quantitative Prediction of Cellular Metabolism with Constraint-Based Models: The COBRA Toolbox v2.0". In: *Nature Protocols* 6.9 (Sept. 2011), pp. 1290–1307. doi: 10.1038/nprot.2011.308.
58. Juan Segura-Aguilar et al. "Protective and Toxic Roles of Dopamine in Parkinson's Disease". In: *Journal of Neurochemistry* 129.6 (June 1, 2014), pp. 898–915. doi: 10.1111/jnc.12686.
59. Kirti Sharma et al. "Cell Type- and Brain Region-Resolved Mouse Brain Proteome". In: *Nature Neuroscience* advance online publication (Nov. 2, 2015). doi: 10.1038/nn.4160.
60. David Siegel et al. "Integrated Quantification and Identification of Aldehydes and Ketones in Biological Samples". In: *Analytical Chemistry* 86.10 (May 2014), pp. 5089–5100. doi: 10.1021/ ac500810r. pmid: 24745975.
61. KatrinStrassburgetal."QuantitativeProfilingofOxylipinsthroughComprehensiveLC-MS/MS Analysis: Application in Cardiac Surgery". In: *Analytical and Bioanalytical Chemistry* 404.5 (2012), pp. 1413–1426. doi: 10.1007/s00216-012-6226-x. pmid: 22814969.
62. Lloyd W. Sumner et al. "Proposed Minimum Reporting Standards for Chemical Analysis". In: *Metabolomics* 3.3 (2007), pp. 211–221. url: http://link.springer.com/article/10.1007/ s11306-007-0082-2 (visited on 03/19/2015).
63. Ruben T'Kindt et al. "Profiling over 1500 Lipids in Induced Lung Sputum and the Implications in Studying Lung Diseases". In: *Analytical Chemistry* 87.9 (May 2015), pp. 4957–4964. doi: 10.1021/acs.analchem.5b00732. pmid: 25884268.

64. Ines Thiele and Bernhard Ø Palsson. “A Protocol for Generating a High-Quality Genome-Scale Metabolic Reconstruction”. In: *Nature Protocols* 5.1 (Jan. 2010), pp. 93–121. doi: 10.1038/ nprot.2009.203.
65. Ines Thiele et al. “A Community-Driven Global Reconstruction of Human Metabolism”. In: *Nature Biotechnology* 31.5 (May 2013), pp. 419–425. doi: 10.1038/nbt.2488.
66. Ines Thiele et al. “Candidate Metabolic Network States in Human Mitochondria. Impact of Diabetes, Ischemia,andDiet.” In: *Journal of Biological Chemistry* 280.12(Mar. 25, 2005), pp. 11683– 11695. doi: 10.1074/jbc.M409072200.
67. Cole Trapnell et al. “Differential Gene and Transcript Expression Analysis of RNA-Seq Experiments with TopHat and Cufflinks”. In: *Nature Protocols* 7.3 (Mar. 1, 2012), pp. 562–578. doi: 10.1038/nprot.2012.016. pmid: 22383036.
68. HiroshiTsugawaetal.“HighlySensitiveandSelectiveAnalysisofWidelyTargeted Metabolomics Using Gas Chromatography/Triple-Quadrupole Mass Spectrometry”. In: *Journal of Bioscience and Bioengineering* 117.1 (Jan. 2014), pp. 122–128. doi: 10.1016/j.jbiosc.2013.06.009. pmid: 23867096.
69. Monica Villa et al. “One-Electron Reduction of 6-Hydroxydopamine Quinone Is Essential in 6-Hydroxydopamine Neurotoxicity”. In: *Neurotoxicity Research* 24.1 (Feb. 6, 2013), pp. 94–101. doi: 10.1007/s12640-013-9382-7.
70. Christina Virgiliou et al. “Development and Validation of a HILIC- MS/MS Multi-Targeted Method for Metabolomics Applications.” In: *Electrophoresis* 36.18 (July 2015), pp. 2215–2225. doi: 10.1002/elps.201500208. pmid: 26180020.
71. Nikos Vlassis, Maria Pires Pacheco, and Thomas Sauter. “Fast Reconstruction of Compact Context-Specific Metabolic Network Models”. In: *PLoS Comput Biol* 10.1 (Jan. 16, 2014), e1003424. doi: 10.1371/journal.pcbi.1003424.
72. Sharon J. Wiback et al. “Monte Carlo Sampling Can Be Used to Determine the Size and Shape of the Steady-State Flux Space”. In: *Journal of Theoretical Biology* 228.4 (June 2004), pp. 437– 447. doi: 10.1016/j.jtbi.2004.02.006.
73. Jenny Marie T. Wong et al. “Benzoyl Chloride Derivatization with Liquid Chromatography1531 Mass Spectrometry for Targeted Metabolomics of Neurochemicals in Biological Samples”. In: *Journal of Chromatography A*

1446 (2016), pp. 78–90. doi: 10.1016/j.chroma.2016.04.006. pmid: 27083258.

74. Takayuki Yamada et al. “Development of a Lipid Profiling System Using Reverse-Phase Liquid Chromatography Coupled to High-Resolution Mass Spectrometry with Rapid Polarity Switching and an Automated Lipid Identification Software”. In: *Journal of Chromatography A* 1292 (May 1537 2013), pp. 211–218. doi: 10.1016/j.chroma.2013.01.078. pmid: 23411146.
75. Min Yuan et al. “A Positive/Negative Ion–Switching, Targeted Mass Spectrometry–Based Meta1539 bolomics Platform for Bodily Fluids, Cells, and Fresh and Fixed Tissue”. In: *Nature Protocols* 1540 7.5 (Apr. 2012), pp. 872–881. doi: 10.1038/nprot.2012.024. pmid: 22498707.
76. L Zecca et al. “Substantia Nigra Neuromelanin: Structure, Synthesis, and Molecular Behaviour”. 154_2 In: *Molecular Pathology* 54.6 (Dec. 2001), pp. 414–418. pmid: 11724917. url: http://w/ww.ncbi. 1543 nlm.nih.gov/pmc/articles/PMC1187132/ (visited on 11/04/2015).
77. Jiangjiang Zhu et al. “Colorectal Cancer Detection Using Targeted Serum Metabolic Profiling”. 1545 In: *Journal of Proteome Research* 13.9 (Sept. 2014), pp. 4120–4130. doi: 10.1021/pr500494u.

5